CURRENT CROWDING EFFECTS ON THE THERMAL PERFORMANCE OF AlGaN/GaN LIGHT EMITTING DIODES

by

Emine Göktepe

B.S., Mechanical Engineering, Yıldız Technical University, 2015

Submitted to the Institute for Graduate Studies in
Science and Engineering in partial fulfillment of the
requirements for the degree of
Master of Science

Graduate Program in Mechanical Engineering
Boğaziçi University

2022

ACKNOWLEDGEMENTS

I would like to express my endless thanks to my dear thesis advisor, Nazlı Dönmezer, for her patience, support, kindness, and guidance throughout my study. I would also like to express my endless gratitude to Mr. Hakan Ertürk for being an excellent teacher and accepting to be a member of this thesis jury. Finally, I would like to thank Mr. İlker Tarı for taking his precious time and joining my thesis jury.

I want to thank my colleagues Onurcan, Haluk, İlke, Canberk, Taher, Pegah, Amir from MinTh Group for their collaboration. I am appreciating to Serdar Kocaman and to his student Selim Gül for letting us use their sources and sharing their valuable knowledge. I am thankful to my friends Aras, Suna, Çağdaş, Günay, and Uğur for their immense support.

I also thank Boğaziçi University Research Funding Organization for their support for our work with grant number 17782.

Finally, I would love to thank my love Görkem Biçen for sharing dreams and facts, good and bad together through this journey.

ABSTRACT

CURRENT CROWDING EFFECTS ON THE THERMAL PERFORMANCE OF AlGaN/GaN LIGHT EMITTING DIODES

In the areas, such as automotive, outdoor, and building lighting in which high brightness is very significant, high lumen AlGaN/GaN light emitting diodes (LED) are preferred due to their low energy consumption vs high intensity light output. Although their high energy efficiency, a large proportion of electrical energy is converted into heat and causes device temperatures to rise. It is important to solve the thermal problems of the devices as the increasing temperatures will affect the properties of the devices such as longevity, lumen flux, and wavelength. The largest heat generation mainly occurs between the p-n junction area where the highest temperature values are observed. All LED luminaire and device designs are possible with accurate detection of junction temperatures. In high lumen applications, non-uniform distribution of current density known as current crowding will affect unexpectedly high junction temperatures may exceed the safe limit and result in degradation in/around thermal hotspots. However, it is very difficult to obtain the junction temperatures of variations at high resolution with current experimental techniques. Junction temperatures can be determined more precisely with multidimensional electro-thermal models by considering the nonuniformities such as current crowding. There are very few studies in the literature where electrical and thermal models are combined. Two-dimensional electrothermal simulations based on finite-element method numerical simulation will be developed to study the electrical and thermal properties of chip level high-lumen LEDs. Junction temperature distribution of LED chips in LED array structures will be obtained considering the effects of current crowding and recombination phenomenon. Hotspot formations in the device structure due to the current crowding effect will be investigated. Simulations will be performed by the commercial software COMSOL Multiphysics Semiconductor Module.

ÖZET

AKIM YOĞUNLAŞMASININ AlGaN/GaN IŞIK YAYAN DİYOTLARIN TERMAL PERFORMANSI ÜZERİNE ETKİLERİ

Otomotiv, dış mekan ve bina aydınlatması gibi yüksek parlaklığın çok önemli olduğu alanlarda, yüksek lümenli AlGaN/GaN ışık yayan diyotlar (LED), yüksek yoğunluklu ışık çıkışına karşın düşük enerji tüketimi nedeniyle tercih edilmektedir. Yüksek enerji verimliliklerine rağmen, elektrik enerjisinin büyük bir kısmı ısıya dönüştürülerek cihaz sıcaklıklarının yükselmesine neden olur. Artan sıcaklıklar cihazların uzun ömür, lümen akısı ve dalga boyu gibi özelliklerini etkileyeceğinden cihazların termal problemlerinin çözülmesi önemlidir. En büyük ısı üretimi esas olarak en yüksek sıcaklık değerlerinin gözlendiği p-n birleşme alanı arasında meydana gelir. Tüm LED armatür ve cihaz tasarımları bağlantı sıcaklıklarının doğru tespiti ile mümkündür. Yüksek lümenli uygulamalarda, akım yoğunluğunun eşit olmayan dağılımı olarak bilinen akım sıkışması beklenmedik şekilde yüksek bağlantı sıcaklıklarına neden olur, güvenli sınırı aşabilir ve termal yüksek sıcaklık noktalarında/etraflarında bozulmaya neden olabilir. Bununla birlikte, mevcut deneysel tekniklerle birleşme sıcaklıklarını ve varyasyonları yüksek çözünürlükte elde etmek çok zordur. Çok boyutlu elektro-termal modeller ile akım sıkışması gibi düzensizlikler göz önünde bulundurularak bağlantı sıcaklıkları daha hassas bir şekilde belirlenebilir. Literatürde elektriksel ve termal modellerin bir arada kullanıldığı çok az çalışma bulunmaktadır. Yüksek lümenli LED çiplerin elektriksel ve termal özelliklerini incelemek için sonlu elemanlar yöntemine dayalı iki boyutlu elektrotermal simülasyonlar geliştirilecektir. LED dizi yapılarındaki, LED çiplerdeki bağlantı sıcaklık dağılımı, mevcut akımsıkışması ve rekombinasyon etkileri dikkate alınarak elde edilecektir. Mevcut akımsıkışması etkisi nedeniyle cihaz yapısındaki yüksek sıcaklık noktaları oluşumları araştırılacaktır. Simülasyonlar ticari yazılım COMSOL Multiphysics Semiconductor Module kullanılarak gerçekleştirilecektir.

TABLE OF CONTENTS

ACKNOWLEDGEMENTS iii
ABSTRACT iv
ÖZET v
TABLE OF CONTENTS vi
LIST OF FIGURES viii
LIST OF TABLES xiii
LIST OF SYMBOLS xv
LIST OF ACRONYMS/ABBREVIATIONS xix
1. INTRODUCTION 1
1.1. Light Emitting Diodes 1
1.2. Thermal and Electrical Reliability of LEDs 7
1.3. Thermal Characterization of LEDs 12
1.3.1. Experimental Techniques 13
1.3.1.1. Forward Voltage Method 13
1.3.1.2. Raman Spectroscopy 14
1.3.1.3. IR Camera 16
1.3.1.4. Thermocouple 17
1.3.1.5. Analytical Techniques 18
1.3.2. Numerical Methods 20
1.3.2.1. Thermal Models 20
1.3.2.2. Electro-Thermal Models 22
1.4. Current Crowding and It's Thermal Effects 24
1.5. Motivation and Outline 28
2. LED DEVICE ELECTRO-THERMAL MODEL 31
2.1. Model Geometry 35
2.2. Material Parameters 37
2.3. Mesh structure 42
2.4. Study details 42
2.5. Model Validation 43

2.6. Conclusion 45
3. LOW TEMPERATURE STUDY 47
3.1. Boundary Conditions 47
3.2. Results 48
3.3. Discussion 55
3.3.1. Thermal approach vs Electro-Thermal studies 55
3.3.2. Temperature Dependent Thermal Conductivity and Specific Heat. 56
3.4. Conclusion 60
4. HIGH TEMPERATURE STUDY. 62
4.1. Boundary Conditions 62
4.2. Results. 63
4.3. Discussion 68
4.3.1. Thermal approach vs Electro-Thermal studies 68
4.3.2. Temperature Dependent Thermal Conductivity and Specific Heat. 68
4.4. Conclusion 69
5. CONCLUSION & FUTURE STUDIES. 71
REFERENCES 73
APPENDIX A: COPYRIGHT PERMISSIONS 83

LIST OF FIGURES

Figure 1.1. Bandgap and visible spectrum for several semiconductor materials [6]. . 2

Figure 1.2. Side and top wievs of Lateral (on the left) and Vertical (on the right) device structures side and top views [9]. License number: 1182899-1 . . 3

Figure 1.3. Schematic representation of particle movement in p-n junctions [6].. . . . 4

Figure 1.4. Cross section schematic representation of an LED with quantum wells [10]. License number: 1182899-1. 4

Figure 1.5. a) Macroscopic illustration of a SQW structure b)band structure of a SQW [11]. License number: 9781118481868 5

Figure 1.6. Demonstration of recombination mechanisms a)SRH, b)auger, and c) direct [14]. License number: 60915. 6

Figure 1.7. Dependency of the lifetime of a LED as a function of the bias current and the junction temperature [16]. License number: 5237120128488. . . 8

Figure 1.8. Spectrum shift due to temperature variation for blue LED [17]. License number: 1183332-1 9

Figure 1.9. Possible current paths between contacts p and n in the GaN Based LED. 9

Figure 1.10. Internal quantum efficiency vs. Current density [16]. License number: 5237120128488. 10

Figure 1.11. Relation between junction temperature and injected current density [29]. License number: 1183336-1. 11

Figure 1.12. Temperature distribution of a LED array for two different array structures via IR thermometry [33]. License number: 1183392-1 12

Figure 1.13. An example of raman test measurement points on a LED [46].License number: 1183361-1. 15

Figure 1.14. Temperature map of a AlGaN/GaN heterostructure field-effect transistor obtained by Raman spectroscopy [47]. License number: 1183362-1. 15

Figure 1.15. Temperature map of a LED by IR Camera [49]. License number: 1183364-1 16

Figure 1.16. Temperature measurement from solder point of LED packaging [51]. . 17

Figure 1.17. Schematic representation of a LED chip packaging thermal resistance map [56] 19

Figure 1.18. Temperature (a) and current density maps for a GaN LED obtained by a fully coupled 3D electro-thermal simulation [32]. License number: 1183372-1. 25

Figure 1.19. Normalized current density profile on lateral direction for altering injection current densities for Lateral squared shape mesa structured LED [87]. License number: 1183373-1. 27

Figure 2.1. Device geometry.. 36

Figure 2.2. Temperature dependent heat capacity of GaN obtained from theoretical calculation (dashed line) and experimental study from literature [88]. . 41

Figure 2.3 Magnified mesh structure.. 42

Figure 2.4. Conduction band energies of electro-thermal models (a) Piprek et al. [73], (b) this study. 43

Figure 2.5. IV curve matching. 44

Figure 2.6. Mesh quality study. 44

Figure 2.7. IV curves from coupled & uncoupled simulations.. 45

Figure 3.1. Electrical and thermal boundary conditions of LED device electro-thermal model.. 47

Figure 3.2. Temperature distribution of LED operating at 7V. 48

Figure 3.3. Total heat generation of device layers for 6V and 7V. 49

Figure 3.4. Total heat generation for 7V, 6V, 5V and 4V applied voltage operation conditions. 50

Figure 3.5. Current density distribution (highest regions are indicated by yellow rings). 52

Figure 3.6. Current density and joule heating on the edge of the second QW at 7V operating condition.. 53

Figure 3.7. Recombination and joule heating at the edge of second QW at 7V operating condition.. 54

Figure 3.8. Current density, joule heating and total volumetric heat generation in zone II.. 54

Figure 3.9. Temperature maps for (a) non-uniform heat generation, b) uniform heat generation applied on entire geometry.. 56

Figure 4.1. The fitting curve and IV curve of the device, fitting curve equation in the box. 63

Figure 4.2. The temperature distribution map for high temperature study at 6V. . . . 64

Figure 4.3. Total heat generation of device layers for 6V high temperature and low temperature studies. 64

Figure 4.4. Total heat generation through the edge of second quantum well. 67

Figure 4.5. Heat generation on the zone II for with heat sink and without heat sink condition. 67

Figure 4.6. Uniform heat generation thermal model for high power study. 68

Figure A.1. Copyright permission for Figure 1.1. and Figure 1.3. 86

Figure A.2. Copyright permission for Figure 1.2. 87

Figure A.3. Copyright permission for Figure 1.4. 91

Figure A.4. Copyright permission for Figure 1.5. 94

Figure A.5. Copyright permission for Figure 1.6. 98

Figure A.6. Copyright permission for Figure 1.7. and Figure 1.10. 103

Figure A.7. Copyright permission for Figure 1.8. 108

Figure A.8. Copyright permission for Figure 1.11. 112

Figure A.9. Copyright permission for Figure 1.12. 116

Figure A.10. Copyright permission for Figure 1.13. 120

Figure A.11. Copyright permission for Figure 1.14. 124

Figure A.12. Copyright permission for Figure 1.15. 128

Figure A.13. Copyright permission for Figure 1.18. 132

Figure A.14. Copyright permission for Figure 1.19. 138

Figure A.15. Copyright permission for Figure 2.2. 144

Figure A.16. Copyright permission for Figure 2.5. 145

LIST OF TABLES

Table 2.1. Hole effective mass parameters [90]. 35

Table 2.2. Layer dimensions & contents. 36

Table 2.3. Conduction band and valence band density of states, electron mass, and hole mass for material layers used in this simulation in 300K. 37

Table 2.4. Heat capacity, thermal conductivity, bandgap, dielectric constant, and doping concentrations used in the model. 38

Table 2.5. Polarization parameters used in simulation. 39

Table 2.6. Mobility parameters for binary material layers 40

Table 3.1. Temperature distribution vs current density distribution. 51

Table 3.2. Quantum well region maximum temperatures calculated by three different methods. 56

Table 3.3. Temperature maps of comparison study for temperature dependent thermal conductivity effect. 57

Table 3.4. Temperature maps for constant and temperature dependent specific heat. 59

Table 3.5. Temperature maps for mixed model and constant thermal parameters. . 60

Table 4.1. Comparison of temperature maps of high and low temperature cases for 5V and 6V.. 65

Table 4.2. Comparison of current density maps of high and low temperature cases for 5V and 6V.. 66

Table 4.3. Comparison of the effect of temperature dependence of thermal parameters.. 69

LIST OF SYMBOLS

a_0	Lattice constant
a_s	Substrate lattice constant
A1	Hole effective mass parameter 1
A2	Hole effective mass parameter 2
A3	Hole effective mass parameter 3
A4	Hole effective mass parameter 4
A5	Hole effective mass parameter 5
B	Direct (Spontaneous) emission coefficient
c	Speed of light
c_1	Heat capacity temperature dependent model parameter
C_n	Auger recombination factor for electrons
c_p	Constant pressure specific heat
C_p	Auger recombination factor for holes
c_{300}	Specific heat at 300K
C_{xx}	Elastic constant
$D_{n,th}$	Thermal diffusion coefficient for electrons
$D_{p,th}$	Thermal diffusion coefficient for holes
e_{xx}	Piezoelectric constants
E	Electric field
E_c	Conduction band energy level
Ec	Reference electric filed for high filed mobility model
E_g	Bandgap
E_v	Valence band energy
E_{trap}	Defect energy level with respect to conduction and valence band
h	Planck's constant
ħ	Reduced Planck's constant
J	Total current density
J_n	Electron current density

J_p	Hole current density
J_f	Forward current
J_s	Saturation current
k	Thermal conductivity
k_{300}	Thermal conductivity at 300K
k_B	Boltzmann constant
L_z	Represents the thickness of the quantum well layers
m_0	Unit electron mass
m_c	Effective electron mass in the conduction band
m_v	Effective hole mass in the valence band
m_{hh}	Heavy hole mass
m_{lh}	Light hole masses
m_{lh}^z	Light hole mass in z-directon
m_{hh}^z	Heavy hole mass in z-directon
m_{hh}^t	Heavy hole mass in transverse direction
m_{lh}^t	Light hole mass in transverse direction
n	Electron density
n_1	High field mobility model exponent of electrical field 1
n_2	High field mobility model exponent of electrical field 2
$n_{i,eff}$	Effective intrinsic carrier density
n_{ideal}	Ideality factor
N_A	Concentration of ionized acceptors
N_D	Concentration of ionized donors
N_c	Effective density of states for conduction band
N_v	Effective density of states for valence band
$N_{c,2D}$	2D effective density of states in the conduction band
$N_{v,2D}$	2D effective density of states in the valence band
P_{tot}	Heat generation in the device
q	Elementary electron charge
$\vec{q}$	Heat flux vector
$\dot{q}$	Heat generation.

$\dot{q}_j$	Joule heat generation
$\dot{q}_a$	Recombination heat generation
p	Hole density
P_{sp}	Spontaneous polarization constant
P_{pz}	Piezoelectric polarization constant
R	Net recombination rate
R_{Aug}	Auger recombination rate
R_{net}	Net generation-recombination rate
R_{Rad}	Direct recombination rate
R_{SRH}	Shockley Read Hall recombination rate
R_{th}	Solder to junction total thermal resistance
$R_{th,J\text{-}C}$	Junction to case total thermal resistance
T	Lattice temperature
T_j	Junction temperature
T_s	LED surface temperature
T_{sp}	Solder point temperature
V_j	Junction voltage
v_{sat}	Saturation velocity for high field mobility model
α	High field mobility parameter
α_k	Thermal conductivity temperature exponent
β	Heat capacity temperature constant
ε	Electrical permittivity
λ	Wavelength
ρ	Density
ϕ	Electrical potential
μ_n	Electron mobility
μp	Hole mobility
τ_n	Electron carrier lifetimes
τ_p	Hole carrier lifetime
σ_{2D}	Net polarization charge densities

μ_0	Low field mobility(electron/hole)
μ_{min}	Low field minimum charge mobility (electron/hole)
μ_{max}	Low field maximum charge mobility (electron/hole)
$\beta 1$	Low field mobility model temperature exponent 1
$\beta 2$	Low field mobility model temperature exponent 2
$\beta 3$	Low field mobility model temperature exponent 3
$\beta 4$	Low field mobility model temperature exponent 4
α_1	Low field mobility model parameter
N_{ref}	Reference charge concentration for low field mobility model

LIST OF ACRONYMS/ABBREVIATIONS

2D	Two Dimensional
3D	Three Dimensional
AlN	Aluminium Nitride
AlAs	Aluminium arsenide
AlGaAs	Aluminium gallium arsenide
AlGaN	Aluminium gallium nitride
EIA	Energy Information Administration
FEM	Finite element method
GaN	Gallium Nitride
GaAs	Gallium Arsenide
InN	Indium Nitride
InGaN	Indium Gallium Nitride
IR	Infrared
LED	Light Emitting Diode
QW	Quantum Well
Si	Silicon
SiC	Silicon carbide
SRH	Shockley Read Hall
U.S.	United States
UV	Ultraviolet
UV-C	Ultraviolet C Band

1. INTRODUCTION

Lighting applications takes an important place in our daily life. We need devices to convert energy into light with the desired wavelength. In recent technology, incandescent, fluorescent, and LED lights are being used for this purpose. Light Emitting Diodes (LEDs) are the most efficient devices that convert electricity in usable form light [1]. Considering the estimation of the U.S. Energy Information Administration (EIA) in the Annual Energy Outlook 2021 that %6 of the total electricity consumption of the U.S. is just for lighting applications [2]. Today, LED luminaires are replacing incandescent light bulbs due to their efficiency and long life. According to the U.S. Department of Energy, LEDs lighting has a high potential for energy saving in the U.S. Their estimation is that by 2027, widespread use of LEDs could save a high amount of electricity which is equivalent annual electrical output of 44 large electric power plants (1000 megawatts each) by 2027 [3]. LEDs are frequently used in automotive, building, and household lighting applications. In addition to lighting applications, these devices are also used in UV disinfecting, infrared imagining, and also additive manufacturing applications.

1.1. Light Emitting Diodes

Nick Holonyak is the person who first introduce the visible III-V alloy semiconductor LED in 1962 [4]. Even though the brightness was very weak compared to incandescent light bulbs, it was a revolutionary triumph. Later, Nakamura fabricated the GaN visible blue LED with which it is possible to create high intensity white light emission [5]. The working mechanisms are quite different compared to the previously invented incandescent and fluorescent lighting types. In incandescent lights, a metal wire is heated up until it reaches to a very high temperature for it to glow. In fluorescent lights current applied through the mercury gas. On the other hand, in LEDs the applied current moves electrons through a solid-state semiconductor material. LEDs require very low energy compared to others to emit the same amount of light. Since no heating is needed, they operate quickly. Moreover, compared to other types, their sizes small and they have a

long lifetime. There is high demand for LED devices due to their advantages over incandescent and fluorescent lamps.

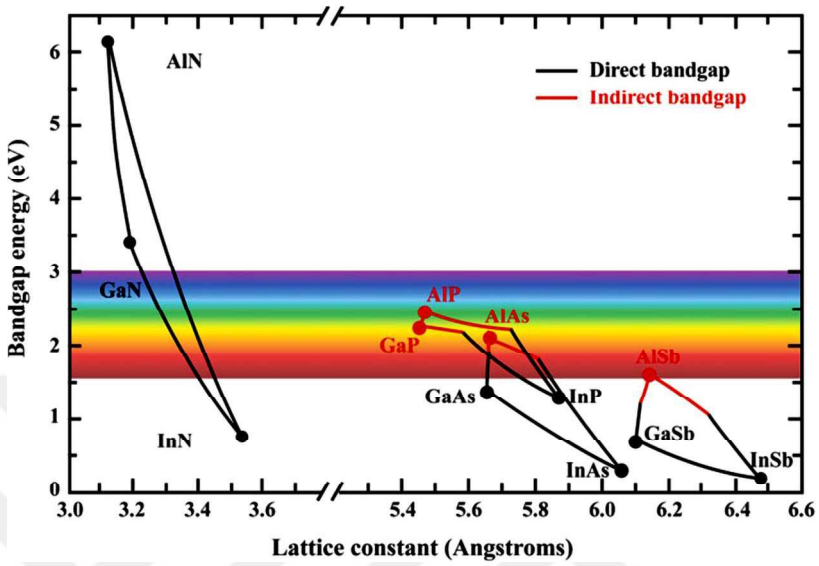

Figure 1.1. Bandgap and visible spectrum for several semiconductor materials [6].

Semiconductor materials such as GaAs, AlGaAs, AlAs, AlGaN, GaN are used for the fabrication of LED structures. Even though light emission can be obtained by many semiconductor materials with a direct bandgap, AlGaN/InGaN alloys are beneficial for creating visible blue/white LED structures thanks to their wide bandgaps. Wide bandgap materials are the materials with bandgaps higher than 2 eV such as AlGaN, GaN, and SiC [7]. For lighting applications, it is necessary to have a compound that has a direct bandgap in the visible wavelength interval. In Figure 1.1 the bandgap energies of several compounds are shown. Figure 1.1. shows that with the compositions of AlN, InN, and GaN it is possible to achieve UV and visible spectrum radiation. In the first studies on this field, it is shown that InGaN LEDs show superior thermal performance compare to other conventional LEDs [8]. Introduction of GaN LED devices triggered to expand the usage areas of LEDs from disinfection to visible white lights with their short wavelength emission in UV band. For example, in the wavelength range UV-C the titanium dioxide photocatalytic air purifying applications. UV LEDs also have been used in applications such as curing of coatings such as glues and inks or the workpiece itself as in the field of 3D printing [9]. In addition, compared to the other UV light emitter fluorescent lamps, they

are both environmentally friendly and provide large wavelength intervals. With all these advantages, AlGaN/GaN LED luminaires are becoming more popular each day.

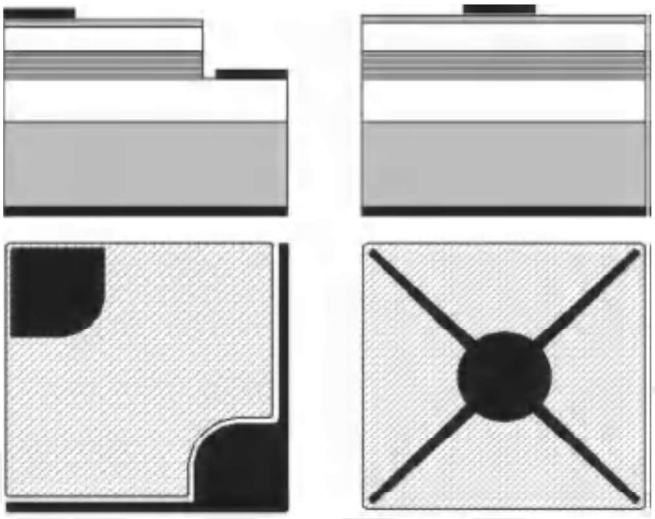

Figure 1.2. Side and top wievs of Lateral (on the left) and Vertical (on the right) device structures side and top views [9]. License number: 1182893-1.

The structure of the LEDs is very basic without any moving parts. LEDs are formed by depositing more than one semiconductor material in thin layers on top of each other. There are two types of main LED architecture that are called vertical and lateral structures. In the vertical devices, generally, a conductive substrate such as SiC is used. In this structure, electrodes are placed on opposite sides facing each other for the vertical flow of electric current from n-contact to p-contact. All the material layers are stacked upon each other. In lateral structures, generally an insulator substrate such as sapphire is being used. Electrodes are placed side by side facing the same direction which leads a lateral current flow. An example of these two main architectures is given in Figure 1.2.

The physics of LEDs can be described as the electron-hole movement through a pn junction. The electrons are positioned on the conduction band and the holes are positioned in the valence band. Basically, charged particles (electrons and holes) are accelerated by applying a voltage difference between p and n junctions. While the electrons tend to move to the positively charged direction, holes tend to move in the cathode direction. On the depletion layer, where the p-type and n-type material intersection, recombination of these particles occurs. Resulting in the dropping of the electrons from a higher energy level to a

lower energy level and releasing their energy in terms of light. An illustration of this phenomenon is shown in Figure 1.3.

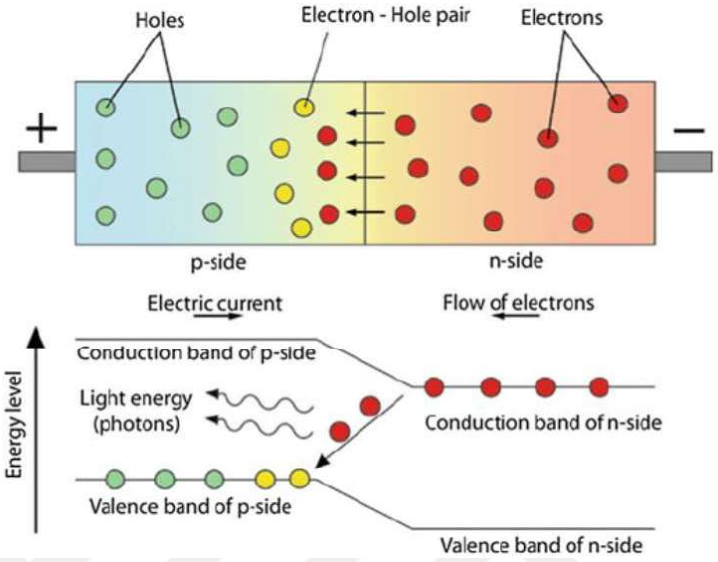

Figure 1.3. Schematic representation of particle movement in p-n junctions [6].

In most of the cases, the energy gap that electrons drop is confined by adding one or a couple of quantum wells into the structure. Cross section view of an InGaN/GaN green lateral LED with quantum well structure growth on sapphire substrate is presented in Figure 1.4. Quantum wells add the ability to determine the wavelength of the emitted light. They also increase device internal quantum efficiency that is the ratio of emitted photons to injected electrons [6].

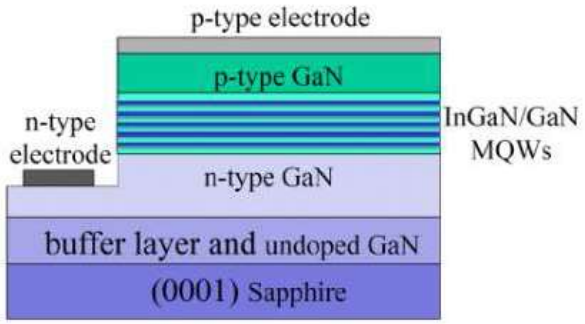

Figure 1. 4. Cross section schematic representation of an LED with quantum wells [10].
License number: 1182899-1.

A schematic representation of a quantum well is given in Figure 1.5. The band structure of this quantum wells is illustrated in the same figure. Because of the difference in energy level of the QW conduction band and barrier conduction band (ΔE_c), the electrons cannot move further along the x-direction. Inside the QW, the concentration of electrons increases, and electrons tend to release their energies while placing in a lower energy level as shown in Figure 1.5.b. Even though the electrons are confined in the z-direction, they are free to move in the x and y-directions. Since these energy levels in QW are discrete, the emitted energy can have certain wavelengths.

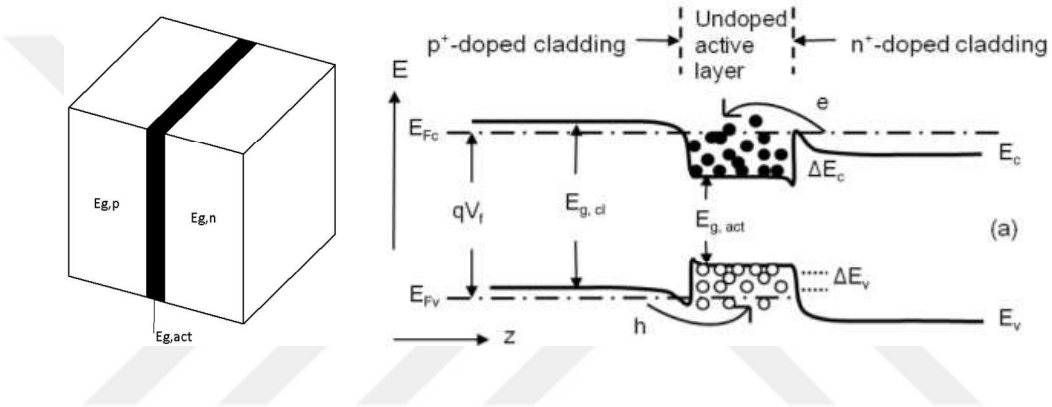

Figure 1.5. a) Macroscopic illustration of a SQW structure b)band structure of a SQW [11]. Licence number: 9781118481868.

The wavelength of the emission can be found by the famous relation given as

$$E_g = \frac{hc}{\lambda} \tag{1.1}$$

where E_g is the bandgap of the material, h is the Planck constant, c is the speed of light, and λ is the wavelength of the emitted light.

While in indirect bandgap materials the electrons release their energy in terms of heat, in the direct bandgap materials electrons releases their energy in terms of heat or light. This phenomenon is called non-radiative and radiative recombination. Recombination is defined as the annihilation or destruction of electrons by Pierret [12, 13]. There are several types of recombination mechanisms that are direct, SRH(Shockley-Read-Hall) and Auger recombination. Generally, the non-radiative recombination is an undesired result of the operation of an LED device.

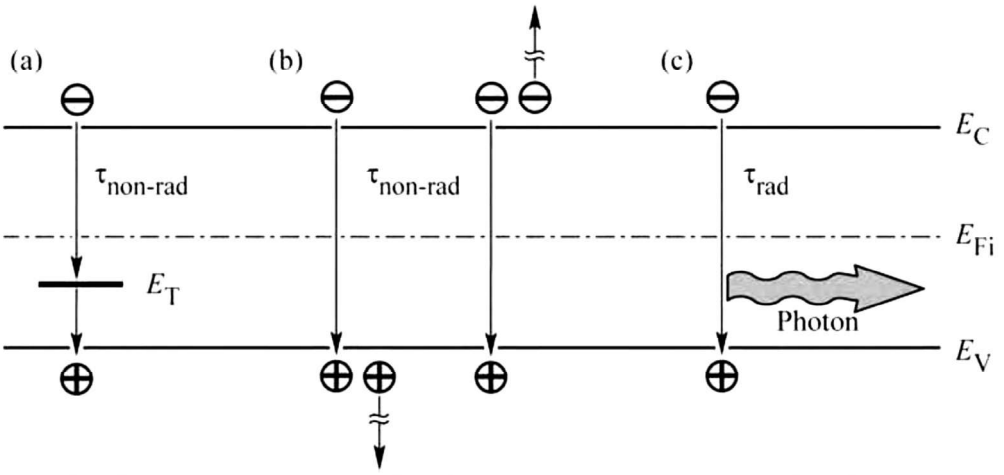

Figure 1.6. Demonstration of recombination mechanisms a)SRH, b)auger, and c) direct [14]. Licence number:60915.

Impurities such as dislocations, foreign atoms, or defects inside the material layers create available trap energy levels inside the forbidden gap of the semiconductor. As shown in Figure 1.6.a, the electrons on the conduction band may be trapped in these impurity energy levels before reaching the valence band holes for radiative recombination. This physics phenomenon is called SRH recombination that is a type of non-radiative recombination.

In auger recombination, the released energy excites the electrons or holes around it and increase their energy level instead of turning to light. Excited carriers with high energies release their energy by vibration, in other words in terms of heat [12]. Auger recombination might be significant in heavily-doped semiconductors [15]. An illustration of auger recombination is given in Figure 1.6.b.

Direct recombination is the main mechanism for light exposure. That is also called the radiative recombination. The amount of light emission is related to electron and hole concentration, that's why radiative recombination occurs higher amount in quantum wells versus bulk material for the same applied current [11]. In the direct recombination, the electron falls from a higher energy state to fill an available hole in the valence band. While falling to a lower energy state, the excess energy is released in terms of light [13]. An illustration of direct recombination is given in Fig 1.6.c.

The sum of all these three recombination rates is

$$R = R_{SRH} + R_{Rad} + R_{Aug} \quad (1.2)$$

that is accounted for the total recombination rate.

1.2. Thermal and Electrical Reliability of LEDs

Due to their promising efficiency and ability to emit high-quality light, LEDs are continuing to be studied extensively. The main effort behind the studies is to further improve the performance of these devices. Although the efficiency of the LEDs is very high with respect to incandescent and fluorescent lighting, their efficiency can only reach up to 40-50% and the rest of the energy is lost in the form of heat [4]. Excessive heat results in undesirable effects that are sometimes irreversible. In LEDs, generally, the largest amount of heat production occurs at the p and n-type junction. This is also the region the main physical event, recombination, occurs. Junction region is also the most sensitive part to excessive temperatures. Accurate detection of the temperature of this region is an important issue for the LED design since high temperatures may cause significant degradation of the device performance.

The effect of junction temperature on the **lifetime** of an LED is shown in Figure 1.7. The figure shows an average of several measurements. According to the data given in the figure, over 120 ºC lifetime of the LED decreases significantly. The same figure also shows the relationship between the applied terminal current and junction temperature. Especially in high lumen LED array applications, a high level of injection current has a booster effect on the junction temperature. Unfortunately, the junction temperature is not uniform along the junction. In general, non-uniform temperature distribution and even hot spot regions are observed in the devices due to non-uniform current distributions.

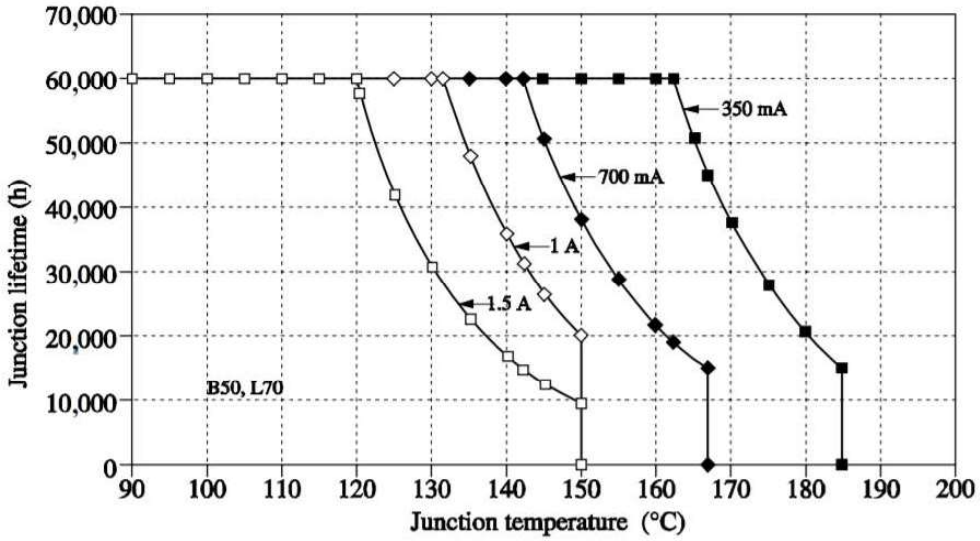

Figure 1.7. Dependency of the lifetime of a LED as a function of the bias current and the junction temperature [16]. License number: 5237120128488.

For many commercial and industrial applications, we need to confine the light in between a specific wavelength interval. Especially for some industries, light sources in between specific wavelength bands is a must. For example, for sanitation and sterilization purposes deep UV wavelength light emitters are being used. The human eye does not have the ability to observe objects in poorly lit environments. In fact, it is only capable of observing objects that are illuminated within a very narrow wavelength band which is called the visible spectrum. As a result, for lighting applications, it is significant that the wavelength of the emission is in the visible range. For IR data transferring, the wavelength of the emission should be in the infrared region. Even though Emission wavelength of an LED is adjusted by altering the material compound ratios in the fabrication process. However, operating at the increasing temperatures affects the wavelength of emission. As illustrated in Figure 1.8. in the study of Ye *e.t al.* [17], when the temperature of the LED device raises, the **wavelength** of the peak emission shifts. Moreover, the intensity of the light decreases. Under high temperature operating conditions, the wavelength of the device might shift to a level that results in a change in the color of the light. Not only temperature but also studies show a shift in wavelength of LEDs due to increasing injection current [8]. To ensure the color quality of the emitted light, operation temperature should retain certain temperature values.

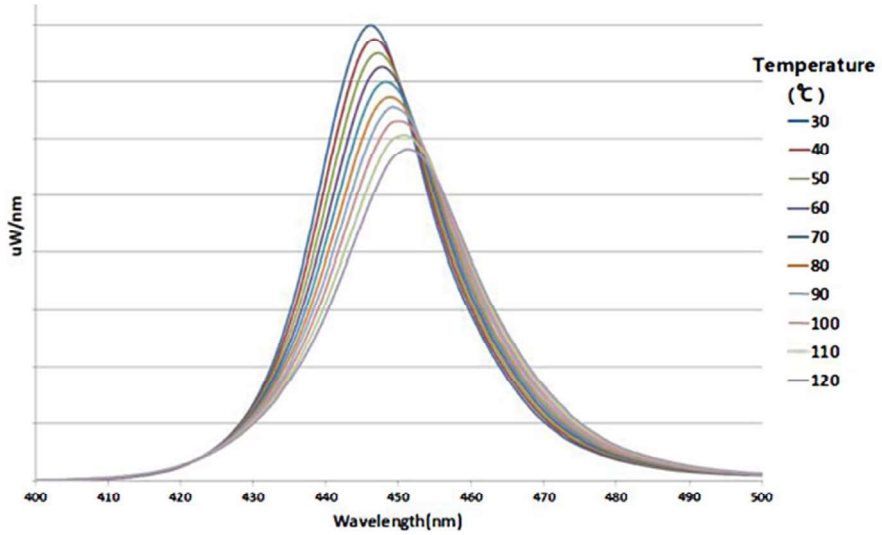

Figure 1.8. Spectrum shift due to temperature variation for blue LED [17]. License number: 1183332-1.

In addition to the thermal limiting factors on device performance, LEDs face a number of electrical issues. For example, electron leakage through quantum wells, contact metal resistance, and current crowding are some of the major electrical problems in LED devices. Some of these electrical factors cause the junction temperature to rise.

In order to optimize the performance of the devices, the current should pass through the entire active area. Figure 1.9. shows the alternative paths on the cross-sectional area of the LED chip.

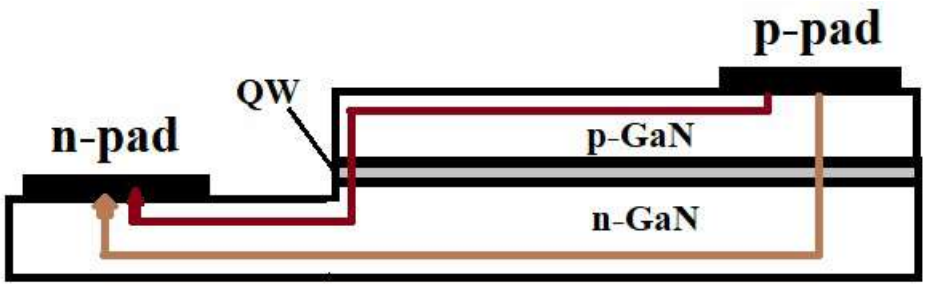

Figure 1.9. Possible current paths between contacts p and n in the GaN Based LED.

Increasing current density results in high current crowding which is one of the main causes of the efficiency drop of LEDs [18–21]. Current crowding is the phenomenon

explained as the high concentration of current density on specific regions within the device layers. The minimum current path resistance emerges in and around these regions especially on high power applications [22]. Even though the lateral device geometries are advantageous for their easy to fabricate nature, they face severe current crowding effects [23, 24]. From p-contact to n-contact, the current follows a lateral direction by resulting current density increase around mesa edges [25]. This phenomenon results in inequalities in the amount of electroluminescence and the heating distribution of chips [26]. In Figure 1.10. the increase of current density enhances the internal quantum efficiency, however, after a specific current density value, current density has a sharp detractive impact on internal quantum efficiency.

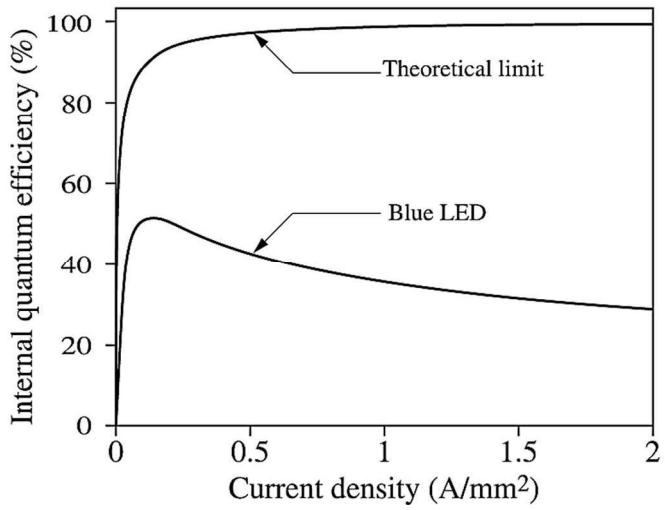

Figure 1.10. Internal quantum efficiency vs. Current density [16]. License number: 5237120128488.

Nonuniform current density distribution may have further adverse effects on device performance. Kim *et. al.* [27] showed the effects of current spreading on the performance of a GaN LED by examining current-voltage relation of the device theoretically. They also showed the effect of applied current density on device lifetime and output power by means of experimental measurements. While current density increases the lifetime of the device decreases. On the other hand, increasing current density has a favorable effect on device output power to a point. After reaching a saturation point, the light output is also being affected adversely. They draw the conclusion that after exceeding the critical applied

current density level, the current crowding occurs in localized regions within the device which leads to the generation of Joule heating that decreases the device lifetime and efficiency. Out of their study, we can conclude to see the current crowding effects on temperature distribution, the device should be operated at high input currents.

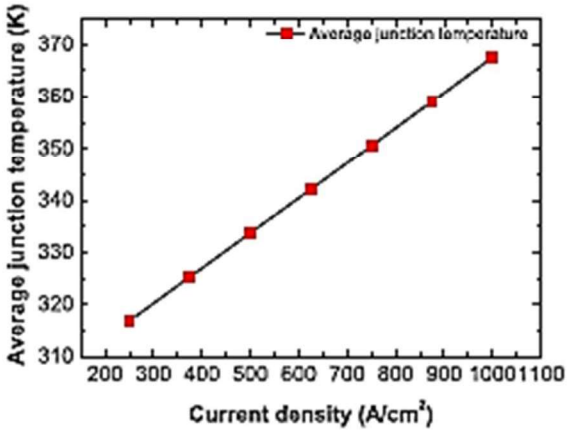

Figure 1.11. Relation between junction temperature and injected current density [27]. License number: 1183336-1.

The boosting effect of increasing current density on the junction temperature is previously shown in many studies [28, 29]. Li *et.al.* presented the linear increase of junction temperature in consequence of the altering current density as in Figure 1.11.

Inhomogeneous distribution of current causes temperature hotspots. Since lateral geometries are generally fabricated on the poor insulating substrate, it is difficult to remove this extra heat from the device [24]. Mostly, the regions that has high current density coincide with the regions with highest temperatures within the device [30, 29].

This direct relation indicates that for the studies related to temperature distribution within the device, characterization of current crowding plays a major role. To accurately detect and plot the temperature map of a device, the current crowding effects should be considered in models.

1.3. Thermal Characterization of LEDs

The intensity and the color of emission depend on many properties such as layer dimensions, doping level, operating temperature, etc. Accurate thermal characterization of the LEDs is significant for proper device selection for desired applications. In many applications LEDs are designed in array structures. Heat sinks are utilized to cool the single and array level applications.

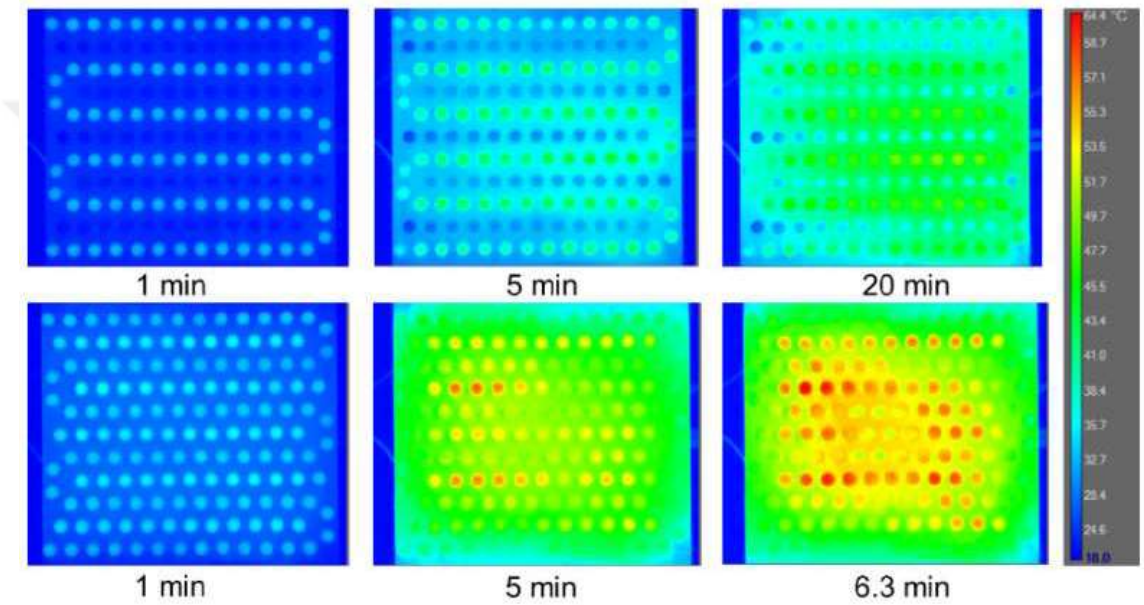

Figure 1.12. Temperature distribution of a LED array for two different array structures via IR thermometry [31]. License number: 1183392-1.

Heat sink dimensions highly depend on the heat generation of the device and junction temperature among several other parameters. In order to keep the device at a certain temperature, it is necessary to be able to fix the base temperature at values close to room temperature. However, in a tightly aligned array design like the comparison in Figure 1.12., where a large number of LEDs come together, the base temperature of the device in the center and the base temperature of the device on the edge are quite different that is much larger in the middle of the structure [31–34]. Accordingly, the amount of heat they lose from the base, so their temperature map will also be different. Since the electrical properties of the LED are highly dependent on temperature, the efficiency of each led will

be also different from each other. Especially in high power applications, the difference between base temperatures is getting wider.

Since these parameters are highly dependent on device temperature, it is significant to accurately characterize the temperature distribution within the device. There are several methods to follow for this purpose. These are measurement techniques, thermal models, and electro-thermal models. A detailed explanation of these methods is given in the following titles.

1.3.1. Experimental Techniques

Measurement of the junction temperature of LEDs is a very wide range of study area due to the number of methods used to determine the approximate junction temperature. As previously stated, the junction is a very thin enclosed region which makes it almost impossible to measure classical thermocouple measurement devices. Therefore, several techniques are invented to accurately estimate the temperature within the junction region. Most of the techniques use the advantage of analytical relations between electrical and thermal parameters. Others, use physical formulations such as the thermal diffusion equation. All the techniques have their own advantages and disadvantages. They also have prior setups to assure the accuracy of measurements. In the following sections, we will present some of the most widely used LED temperature measurement techniques.

There are many studies in the literature that compare the available measurement methods to obtain the most accurate results [35, 36]. According to these comparison studies, the forward voltage method is found the most accurate model among these methods. However, it is expensive and time-consuming.

1.3.1.1. Forward Voltage Method. The forward voltage method makes use of the Shockley equation given as

$$J_f = J_s \left(exp \left(\frac{eV_j}{n_{ideal} k_B T} \right) - 1 \right) \tag{1.3}$$

defines the current voltage relationship for an ideal diode [14] where J_f represents forward current, J_s saturation current, V_j junction voltage, n_{ideal} is the ideality factor ranging from 1 to 2, k_B Boltzmann constant, and T is the lattice temperature. From the modified Shockley equation, following the presented steps by Xi. *et. al.* [37], the relationship between the forward voltage and temperature can be found.

The measurement method includes two processes one of which is a calibration step in a temperature-controlled environment. At this step, the device is placed into an oven till it reaches a thermodynamic equilibrium with the environment that is reported varying hours in several studies [38–40]. The equilibrium assures that oven, junction and the overall device have the same temperature. To observe the voltage temperature relationship, a very small current pulse is being applied for different oven temperatures. The aim of the calibration step is to create a forward voltage drop vs oven temperature graph

Afterward, the device is being placed in a room-temperature environment for the second step of the measurement process. The device this time being operated under altering injection currents and resulting voltages are being measured on steady-state. Lastly, the junction temperatures for each injection current value are being calculated from the already achieved relation between Junction temperature-forward voltage data obtained in the first measurement step.

Even though this method is widely used, it is only capable of measuring the average temperature distribution through the junction. In other words, it is not possible to observe temperature hotspot regions with this method.

1.3.1.2. Raman Spectroscopy. Raman spectroscopy is a method that has been used for a long time for the determination of the hotspot regions which is not possible via thermocouples [41]. The method enables to measure on a very small scale. An example of a Raman laser pointer on a LED surface is given in Figure 1.14.

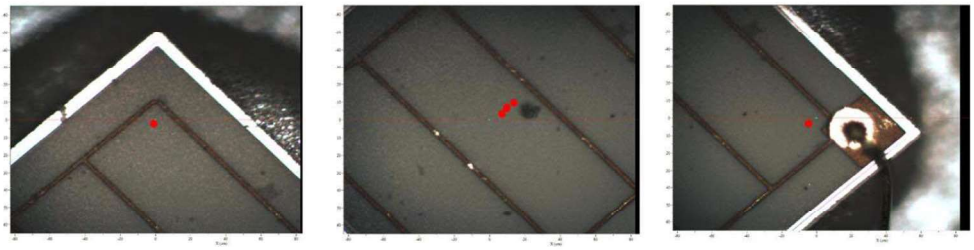

Figure 1.13. An example of raman test measurement points on a LED [42]. License number: 1183392-1.

Raman spectroscopy is used for obtaining the temperature of a sample by examining the reflections of the rays from the sample that are directed from a laser source. When a laser is shined to a sample, the reflection of the photon either gains energy, loses energy, or remains with the same energy. If the energy of the phonons inside the sample is higher than the exposed photon then the reflected photon gains energy and shifts to a lower wavelength band which is called the blue shift. If the energy of the phonons inside the sample is lower than the exposed photon then the reflected photons lose energy and shifts to a higher wavelength band which is called the red shift. By examining these reflected light beams, from the difference between the emitted and reflected laser rays, the temperature of the sample is found. The method is used for not only LEDs but also other semiconductor devices. An example of a temperature map obtained by Raman spectroscopy for an AlGaN/GaN heterostructure field-effect transistor is given in Figure 1.15. Even though this method is useful to determine the temperatures, it is a very expensive measurement method. Necessitate complex experimental setup.

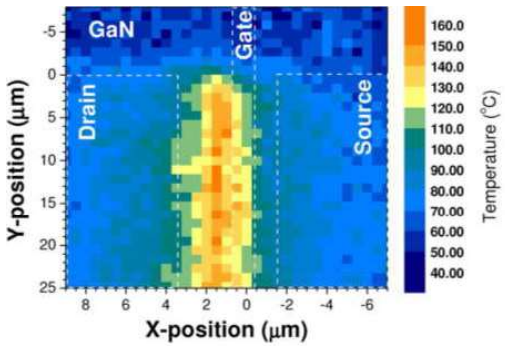

Figure 1.14. Temperature map of a AlGaN/GaN heterostructure field-effect transistor obtained by Raman spectroscopy [43]. License number:1183362-1.

1.3.1.3. IR Camera. IR camera measurement is a non-contact, non-destructive temperature measurement method that makes use of emitted IR radiation from the sample. According to Stefan-Boltzmann law, any material over 0K emits light proportional to its own temperature and emissivity [44]. Even though the peak wavelength of the emitted radiation varies depending on the material and its temperature, it is known that any object over 0K also emits IR radiation. By detecting the emitted IR emissions from objects, it is possible to determine their temperature.

Unfortunately, this method is only capable of obtaining the surface temperature of the sample. Therefore, to reach the temperature distribution below the surface, additional efforts are needed. In addition. IR thermometry results depend heavily on the surface properties of the measured sample such as emissivity and roughness. Moreover, the complication of this methods increases when the emissivity of the measured sample is highly dependent on temperature. Calibration of these equipment takes an important place in the measurement process. Some studies have reported discrepancies between IR measurement results and others [35].

An example temperature map of an experimental study conducted by IR thermometry is given in Figure 1.16. Localization of temperature in the middle of the device is vividly visible. Unfortunately, this method is capable of interpreting of the top surface of the device. For the vertical direction cross-section other methods should be used.

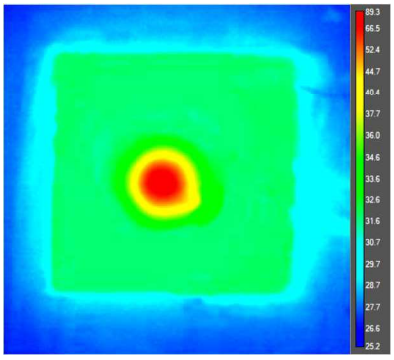

Figure 1.15. Temperature map of a LED by IR Camera [45]. License number: 1183372-1.

1.3.1.4. Thermocouple. Thermocouples are used for direct measurements from material surfaces. This measurement method is the most simple, cheapest, therefore a widely used technique in our daily life from healthcare to scientific purposes. Thermocouples are used in the LED industry for junction temperature measurements [46–48]. These devices are invented based on to thermoelectric effect principle. They are made up of two different metal wires that their tips joint. While one side of the joint is heated up and the other one is kept cool, a voltage difference occurs between two tips which is proportional the temperature difference between two tips [49].

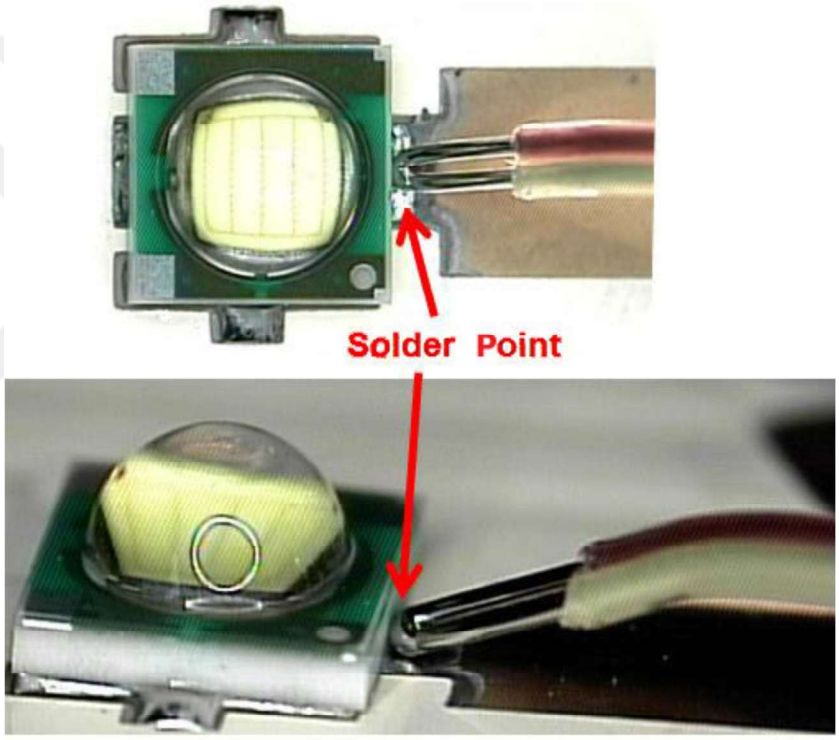

Figure 1.16. Temperature measurement from solder point of LED packaging [47].

Unfortunately, dimensions of the tip of these devices are almost big as the LED chip itself. As can be seen in Figure 1.17., temperature measurement is conducted on a very wide area and too away from the junction point where the region should be measured. Therefore, some analytic relations such as

$$T_j = T_{sp} + R_{th} \times P_{tot} \qquad (1.4)$$

are developed to determine the junction temperature from solder temperature. In the Equation (1.4), T_j represents the junction temperature, T_{sp} solder point temperature, R_{th} solder to junction in K/W unit and P_{tot} is the heat generation in the device. Even though this method is very simple it only gives an average value of junction temperature. Besides, depending on the position and the absorption coefficient of the tip of the thermocouple the measurement results differ a lot [50]. In addition, it weakly estimates the electrical effects such as current crowding and assumes the generated heat is distributed uniformly throughout the device.

Some studies focused on the improve the ability of this conventional measurement method. Lee *et. al.* [51] purposed a technique to identify the junction temperature by using triple measurement points on chip surface, on the solder joint, and on the substrate. They used IR thermometry and wire thermocouples for measurement and compared their results with the transient thermal measurement method. They created empirical equations that correlate junction temperature with the temperatures measured at the aforementioned points based on the observations from FEM numerical study. Their study is a good example of non-localized heating within the device since the temperature of all selected points shows different relations between altered injection current. However, this study does not include a detailed investigation in the distribution of junction temperature in the active region. Also, the simulation method they are used electrical resistance which is generally assumed constant through the device layers. So, as in this study, we need to build empirical correlations and assumptions to achieve junction temperature out of surface temperature measurements.

1.3.1.5. Analytical Techniques. The thermal resistance method is also used for quick estimation of junction temperature in which heat diffusion in a slab assumption is utilized. This model gives a 1D assumption of Fourier's heat conduction law given as

$$R_{th} = \frac{T_j - T_s}{P} \tag{1.5}$$

where R_{th} is the total thermal resistance from the solder to the junction, T_s is the solder temperature and P is the total heat generation within the device. The given equation is a

general demonstration of the thermal resistance model. This model can be applied to any number of device layers by taking the correct boundary conditions and calculating the total thermal resistance of these layers. In Figure 1.18., a schematic representation of an LED with detailed case layers is given. Depending on the positions of the reference point we can define the total thermal resistance of layers. As can be seen in this figure, $R_{th,J\text{-}C}$ represents the total thermal resistance from junction point to outside case of package. Similarly, $R_{th,J\text{-}S}$ represents the total thermal resistance from junction to solder point. In both cases the total heat generation of LED chip and junction temperature terms are the same, but total thermal resistance and the T_s surface temperature differ. The thermal resistance of commercial LED devices provided in the product data sheets are often calculated without concerning the current crowding effect and assumed as constant.

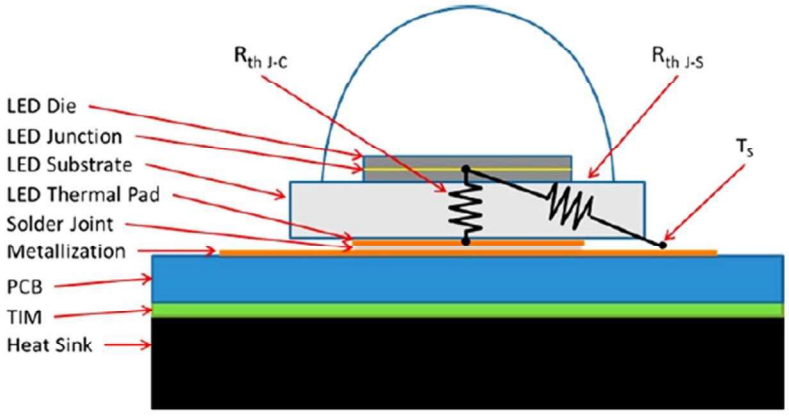

Figure 1.17. Schematic representation of a LED chip packaging thermal resistance map [52].

Thermal resistance models are being widely used [33, 51, 53–55]. These studies aim to calculate the maximum allowable base temperature for LED chip when it is fixed on a heat sink to operate. They use this design condition to optimize the heat sink materials and dimensions. In general, the thermal resistance provided from the LED chip manufacturer datasheets are used to calculate the junction temperatures.

Thermal resistance can be used with both measurement results and thermal models for the detection of junction temperature without requiring a detailed thermal analysis of the device [56]. However, using this data is not suitable for high lumen led applications

because they do not take into account the temperature-varying thermal conductivity effects and current crowding may be crucial for high powers.

1.3.2. Numerical Methods

Equations that describe the physics of semiconductor devices are spatially dependent and highly non-linear equations. These are difficult to solve analytically [57]. For this reason, numerical methods are preferred. In this section. A brief representation of the two models is given.

1.3.2.1. Thermal Models. Thermal models utilize the thermal diffusion equation that is given in Equation (1.6). This model enables 2D and 3D simulations with which Temperature distribution inside the device can be vividly simulated. Heat conduction in a medium is determined by Fourier's law of heat conduction which states that heat flux is proportional to the negative temperature gradient given as

$$\vec{q} = -k.\nabla T \tag{1.6}$$

where $\vec{q}$ is the heat flux vector, k is the thermal conductivity of material and T is temperature. Dissipation of heat within the domain is given by the heat diffusion equation that is

$$\rho c_p \frac{\partial T}{\partial t} = \dot{q} + \nabla.(k\nabla T). \tag{1.7}$$

where ρ is density, c_p is constant pressure specific heat and $\dot{q}$ is heat generation. In an LED device, the main source that generates heat is the current that passes through it. In the heat conduction equation, the effect of electricity is given with the term $\dot{q}$. Heat generation terms will be obtained from electrical simulations.

In a LED device, the heat source $\dot{q}$ mainly consists of two heat generation mechanisms. First the Joule heating due to the thermal resistance of the materials that form the layers (especially p-GaN), designated as $\dot{q}_j$. Secondly, the energy cannot be converted

to light due to nonradiative recombination heat in the active layer, designated as $\dot{q}_a$. The total contribution can be written as

$$\dot{q} = \dot{q}_j + \dot{q}_a. \tag{1.8}$$

In thermal models, the heat generation term is generally assumed constant and applied to the geometry as a boundary condition or a uniform heat generation throughout the body. In other words, the hotspot regions due to local heat generation caused by current crowding and non-radiative recombination are not considered. Since this model does not take the non-uniform heat generation into account, it is limited by the user's viewpoint of determining the heat generation regions which necessitates a perfect knowledge of the electrical and the thermal behavior of the device. This is almost impossible since the heat generation regions are dependent on several parameters and besides the amount of heat generated, finding the thermal diffusion spread length is also a major difficulty to overcome. In general, there are applications that apply volumetric heat generation, from the junction, base point, or all around the device uniformly. However, these assumptions weakly estimate the real device thermal behavior. Even though simulations give the temperature map through the device, it is not accurate.

Studies use the diffusion heat transfer equations by employing 2D or 3D numerical simulations to estimate the junction temperature [53, 58–63]. Some of these studies model the chips as one bulk material (generally Si or GaN) and simulate the heat sink together with the array of bulk chips as heat sources applied to the chip domain, to the top, or to the base of the chip [53, 58–62]. Others directly employ the thermal diffusion equation on a single chip with several layers that heat generation applied one of the layers [63].

However thermal models are coarse assumptions for chip thermal characterization. In the thermal models, variation of temperature dependent properties is neglected and the non-uniform heat generation as a result thermal hotspots are not considered. Moreover, in most of them, the chip is considered as a bulk material that has the same properties on each point. Therefore, even though they are computationally cheap and fast, for accurate characterization they are not suitable. To achieve an accurate heat generation profile and

hotspot formation, the device characteristic temperature dependent parameters should be detailly analyzed by electro-thermal models.

1.3.2.2. Electro-Thermal Models. The actual junction temperature is higher than the value calculated by the thermal resistance method [64]. Furthermore, the capability of thermal models on estimating the device thermal behavior decreases for the high-power devices that operate with high current densities. In this case, electro-thermal models give promising results.

The drift-diffusion equation is derived from the Boltzmann transport equation [65]. It is frequently used for electrical and electrothermal modeling of semiconductor devices such as LED, diodes, and transistors. This equation describes the motion of electrons and holes under the effect of the applied electric field [66]. The electro-thermal simulations couple the Drift-diffusion, Poisson's, and Heat Transfer equations [22, 23, 67, 68]. Poisson and charge continuity, current density, and heat diffusion equations are given as in order

$$\nabla.\varepsilon\nabla\phi = -q(p - n + N_D - N_A) \tag{1.9}$$

$$\nabla.\overrightarrow{J_n} = qR_{net} + q\frac{\delta n}{\delta t} \tag{1.10}$$

$$-\nabla.\overrightarrow{J_p} = qR_{net} + q\frac{\delta p}{\delta t} \tag{1.11}$$

$$\overrightarrow{J_n} = -qn\mu_n\nabla\phi + \mu_n k_B T\nabla n \tag{1.12}$$

$$\overrightarrow{J_p} = -qn\mu_p\nabla\phi + \mu_p k_B T\nabla p \tag{1.13}$$

$$\rho c_p\frac{\partial T}{\partial t} = \dot{q} + \nabla.(k\nabla T). \tag{1.14}$$

In Equation (1.9) ε is defined as the electrical permittivity, ϕ is electrical potential, q is the elementary electron charge, n, and p electron and hole densities, N_D and N_A concentration of ionized donor and acceptors respectively. In addition, in Equations (1.10) and (1.11) J_n and J_p represent the current densities resulting from the motion of positively and negatively charged particles. R_{net} is electron-hole net generation-recombination rate,

μ_n ve μp electron-hole mobilities. In Equation (1.14) ρ, c_p, and k represent density, specific heat, and thermal conductivity respectively. However, this approach is suitable for systems whose characteristic length is fairly long (approximately for macro geometries their characteristic length is larger than 1 um), isothermal and for the cases that applied voltage is lower than 1 V [69, 70]. Furthermore, these equations are applicable to simple and position independent semiconductor band structures that use Maxwell statistics [71, 72]. However, in this study, our device has more than 1 quantum well that are in nm scale and has material parameters highly dependent on lattice temperature. Besides, there is a high amount of localized heat generation due to operation. Therefore, we need to use an appropriate approximation to accurately simulate the device's behavior. The constitutive equations will be provided in the following section.

The electrothermal models are useful to model semiconductor devices to identify the electrical and thermal behavior during the physical activity. In literature this model widely used for electrical characterization of LEDs. One of the most valuable contributions is by Piprek *et. al.* [73] analyzed the electrical and thermal behavior of a Fabry Perot UV laser light emitting diode at maximum output power. In their study, they have illustrated material and operating condition dependent characteristic behaviors that are specific to the device. In their model, they achieved a good agreement with the measured IV curve. This shows the reliability of the model. They compared the maximum output power in cases with and without polarization and achieved that the maximum output power does not change with de polarization effect. They reported a strong joule heating on the p side of the device that limits the optical gain. They also showed that maximum output power increases if the heat dissipation within the device is improved. They explain this phenomenon by comparing two different total thermal resistance cases one of which is fairly small. They resulted that effective removing heat from the device increases the maximum power the device can achieve. In a different study, Piprek *et. al.* [7] investigated the physics and the performance of another UV LED to detect the internal performance limiting mechanisms by a 3D numerical simulation, optical and electrical measurements. For this purpose, they focused on effects such as current crowding, carrier leakage, and polarization. They showed change of electroluminescence at different operating currents, with and without polarization. They revealed that built-in polarization has no significant effect on the wavelength shift of the device, however, it has a strong lowering effect on device peak

emission intensity and emission power. They also investigated the SRH recombination lifetime and band offset ratio effect on the performance of the device. They found decreasing the SRH lifetime and band offset ratio has an adverse effect on internal quantum efficiency. Current crowding is observed near the n-pad edge of the device. Characteristic properties such as recombination rates and electron-hole densities are plotted in two vertical directions that are on the middle axis and on the corner of the device where the minimum and the maximum current densities are observed respectively. They revealed that the SRH recombination rate around the QW region increases significantly (around the order of magnitude 5) on the maximum current density region.

These studies show that with the electro-thermal models, we can obtain very detailed information about the device that is not possible to achieve by aforementioned methods.

1.4. Current Crowding and It's Thermal Effects

One of the main electrical concerns that leads to inefficient device operation is current crowding. Eliminating such effects can only be possible by accurate identification of the strength of current crowding and the regions it occurs. Studies in the literature have focused on accurately examining and characterizing such negative effect in detail. Studies showed that as well as resulting the junction temperatures to increase, current crowding can be boosted by an increase in temperature. Therefore, thermal management may play an important role in device performance. There are plenty of studies investigating these two phenomena.

Sato-Iwanaga *et. al.* [30] investigated the temperature dependent efficiency degradation mechanism of an LED with two different GaN layer thickness cases by employing a three dimensional fully coupled electro thermal simulation. They investigated the relation between current crowding and localized joule heating as one of the main contributors to device efficiency degradation. They showed that when the GaN substrate layer is designed thicker (100 um), the maximum current density in the same region decreases, so the joule heating and junction temperature decreases. They illustrated that the high current density regions and the hot spot regions coincide when the GaN layer is thin

(5um). When the thickness is 100 um the current density effect decreases, the hotspot region shifts to the p side region.

Malyutenko *et. al.* [74] presented the negative effects of current crowding on the thermal map and the light emission of the LEDs by employing optical measurements and Comsol simulations for two vertical chips with different p electrode designs. Study shows that at lower currents heat and light emission distributions are quite uniform, however, at high injection currents they concentrate under the p contact where the vast amount of nonradiative recombination loss occurs.

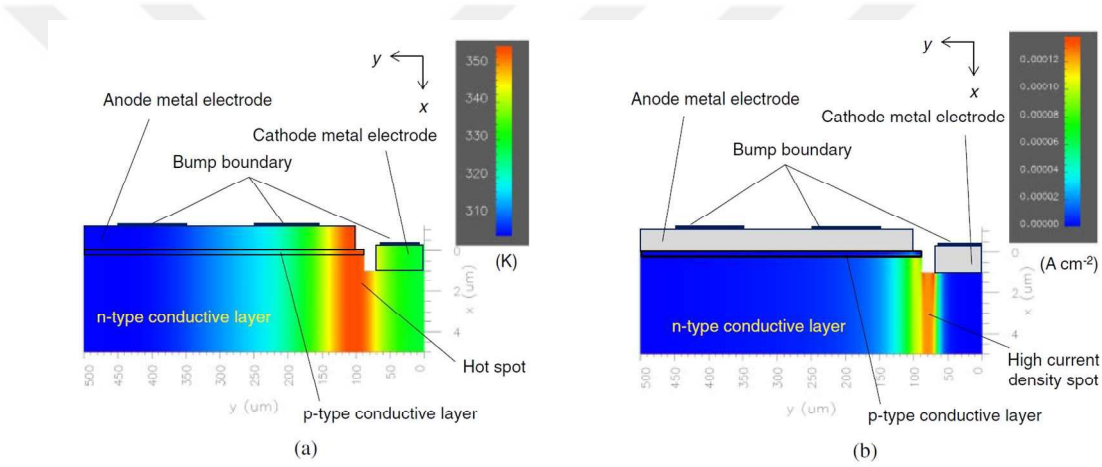

Figure 1.18. Temperature (a) and current density maps for a GaN LED obtained by a fully coupled 3D electro-thermal simulation [30]. License number: 1183372-1.

Othman *et. al.* [75] have compared two LED device geometry respectively vertical and lateral in terms of strength of current crowding phenomenon and its effect on device performance by utilizing a 3D electro-thermal model. They observed a better light output for vertical devices compared to lateral ones mainly because of the current crowding that occurs at and around mesa edges in lateral LEDs. They reported that the heat generation region coincides with the regions that current crowding emerges. Even though this study gives an idea about the structural ground for the formation of current crowding, and its effect on heat generation the study does not comprise high current applications and the effect of thermal boundary conditions.

Most of studies aim to reveal the effective parameters on current crowding and improving them. It has been discovered by many studies that the geometry of the device is a very important factor in the current distribution. Wang *et. al.* [76] investigated the effect of EBL on device electrical and thermal characteristic. They showed that for the case without an AlGaInN EBL the difference between the main heat generation mechanisms is small, but joule heating outbalances the non-radiative recombination heating. For the case with EBL, they observed that non-radiative recombination heating dominates the joule heating. They present that especially at high current density operations this difference becomes larger. Hwu *et al.* [77] investigated the effect of introducing an electron blocking layer into the device geometry and altering n-GaN layer thickness on behavior for a vertical LED chip by a self-developed numerical solver. They used an electrical resistive approach derived from the Shockley equation. According to their study, on a vertical LED chip, the current crowding emerges under the n electrode at high applied current densities. They placed blocking layers below the n-pad with the same size of n-pad right under the p pad and observed that the current blocking layer effectively spreads the current to the regions away from the n-pad so has a decreasing effect on temperature. They remark that on the center of the chip where current crowding is high, the temperature is also maximum as a significant indicator of joule heating. These studies indicates that the EBL layer has a reducing effect on current crowding.

Another widely investigated geometrical parameter in the literature is the electrode design. Hwu *et al.* [77] observed that while n contact dimension increases, the current density in the lateral direction becomes more uniform, so does the temperature distribution. Cao *et. al.* [78] Employed 3D electro-thermal simulation to improve current spreading through a lateral device with different geometries of indium thin oxide patterns on p-GaN. Shim *et.al.* [79] proposed a 3D circuit resistance electrical model to investigate the current spreading in a lateral blue LED by focusing on the metal electrode design and improvement. According to their measurement and simulation results, for the case that the p-electrode is surrounded by the n-electrode a better current density distribution achieved. Hao *et. al.* [80] modeled four flip chip UV LEDs with different p-type contact patterns and achieved higher quantum efficiency with the stripped p-electrode pattern which is the case that also has the most uniform current density distribution. Wang *et. al.* [81] have investigated the resistance of the p-electrode on the current crowding of an LED by

reducing the thickness of the p-electrode into the direction of n-electrode for three different electrode geometries. Reducing the thickness of the p electrode increases its electrical resistance in a way that electrons do not tend to follow. As a result, they achieved a better performance in light output and operating temperature for a low conductive p-electrode design. These studies show a strong relation between electrode design and current crowding. What can be deduced from these studies is that electrode design may give an idea about the possible current crowding formation within the device.

In certain mesa structures, current crowding effects are less observed. Guo *et. al.* [82] proposed LEDs with different mesa geometries to investigate the current density distribution within the device. The p and n contact areas were the same amount in both cases. They showed that the current crowding is high on the n-contact side of the mesa edge for stripped geometry LED. It decreases in ring-shaped geometry, so the light output power increases as well. Shatalov *et. al.* [83] employed a numerical circuit resistance model and experiments to investigate the mesa geometry on current crowding in deep UV AlInGaN LEDs. They showed that squared shaped has higher resistance, so that it also has higher current crowding. The resulting normalized current density profiles on lateral direction for the squared shape mesa is provided in Figure 1.22. Figure shows that increasing injection current density results non-uniform current density distribution.

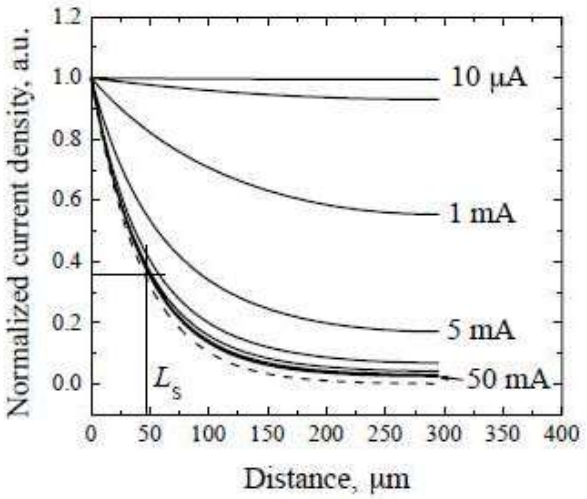

Figure 1. 19. Normalized current density profile on lateral direction for altering injection current densities for Lateral squared shape mesa structured LED[83]. License number: 1183373-1.

Han *et. al.* [84] investigated the effect of current crowding on light extraction of LEDs with two different electrode types. They employed a 3D electrical resistance model to simulate the device and charge coupled device camera to measure light extraction to investigate the relation between optical performance and current crowding. They also measured the device surface temperatures by IR technology. They observed in quantum well layers, around the regions that are high current density occurs, the light intensity is also higher. Besides, for the n-GaN layer, the regions that high current density occur are the same as the regions where the maximum temperatures are observed. They resulted with that in this lateral device type current crowding is the dominant effect on temperature distribution. They also add that since inside the quantum well layers the regions that high luminous intensity occurs do not coincide with intensive current density, they conclude that heat generation in QWs does not play a significant role as much as heating in the n-GaN layer.

Huh *et al.* [9] introduced an insulation silicon dioxide current blocking layer right under the p pad to prevent current crowding under the p-pad and as a result improved the light output power.

These studies give background knowledge to predict the efficiency degradation mechanisms and hotspot regions within the device. Predicting the hotspots regions in a LED geometry might be possible by taking the advantage of the relation between current crowding and joule heating. Studies employing both thermal and electrical methods provide solid information for this relation. Unfortunately, there are very few electro-thermal modeling studies in the literature with devices operating at high currents and temperatures. Besides, the effects of temperature are not discussed in detail in these studies. Conducting a detailed study on the thermal effects on the device is important in terms of enriching the literature.

1.5. Motivation and Outline

In this thesis, the electrical and thermal behavior of a lateral UV laser LED device with altering operating conditions is examined. Some of the electrical and thermal characteristics of this device are priorly investigated by Piprek *et. al.* [73]. In addition to

this study, we also detailly investigated the current crowding effect on device thermal behavior which is previously reported in the literature as an important boosting effect on heat generation within the device. Here we employed fully coupled 2D electro-thermal simulations via COMSOL Multiphysics's Semiconductor Module. We presented the resulting temperature maps, high temperature regions by examining the relation between current crowding, non-radiative recombination heat generation, joule heating, and temperature distribution.

Improving the efficiency of light emitting diodes is essential for the effective usage of our natural energy sources. There have been many studies conducted for improving the performance of LEDs. To be able to improve the efficiency and achieve good thermal management, at first the device's electrical and thermal characteristics should be defined accurately. In the literature, there is a continuous effort for further analyzing the LED device behavior. Especially in high lumen applications heat generation inside the device leads junction temperatures to rise which ultimately brings the device failure.

The Electrical and the thermal behavior of an LED depends on several complex material and geometrical parameters. Therefore, there is a large room to study the effect of parameters on the behavior and performance of these complex devices. Studies on thermal and electrical characterization of LEDs revealed several effective mechanisms behind device degradation and efficiency drop. One of the main concerns stated in the literature is the current crowding effect.

Current crowding and the effective parameters on the formation current crowding have been studied in detail in the literature. However, number of studies are not sufficient to estimate the exact region and strength of current crowding on a complex LED device. Therefore, estimating the thermal behavior that is generally linked to electrical behavior of the device is not possible without employing electro-thermal models. Even though the effect of temperature on current crowding pointed out some studies, the effect of temperature distribution, temperature dependence of thermal parameters, and the change of thermal behavior with altering operation power is not detailly investigated.

Plenty of studies conducted on LED performance do not include the temperature effects for low power operating conditions. However, it is not clear at which power temperature is becoming an effective parameter on device performance. There are studies that utilize thermal and electro-thermal models for the accurate characterization of chip thermal behavior. However, many of them assume a constant temperature device domain while fitting the IV curve. These studies do not consider comparing the environmental altering boundary condition effects such as base temperature. On the other hand, because of the thermal interaction between the LED chips in an array structure, each chip exposed different base temperatures. There are lacking information in the literature for the effect of such difference in boundary conditions on device behavior.

The thermal resistance method is highly used in applications for armature design and array structures. Furthermore, industrial companies stick to this method for its ease of use and its computationally cheap nature. Moreover, for high power LEDs thermal and electrothermal models' comparison for the ability of characterize the temperatures accurately is not clearly investigated. In addition, the electrothermal studies utilize constant thermal conductivities while thermals use temperature dependent. It is a question that what if electro thermal models also employ the temperature dependent conductivity.

In our study we investigated these unclear points in the literature. In the second chapter, the details of the model are given. In the third and fourth chapters, thermal behavior and current crowding effect are examined at low and high temperature operating conditions respectively.

2. LED DEVICE ELECTRO-THERMAL MODEL

LEDs are very complex electrical devices in terms of both their structures in nanometers scales and physical mechanisms within the device. Compared to the same kind of semiconductor devices such as diodes and transistors, they have many more additional layers that affect each other both mechanically and thermally. Even though basic semiconductors can be modeled via the general drift diffusion approach, to be able to simulate the changing electrical fields, the effect of particle movements in nanoscales, position dependent band structure, constitutive equations should be introduced in need for further improve the drift diffusion approach.

COMSOL Multiphysics can simulate such device behavior even though some limitations such as assuming a parabolic band structure and taking the carrier temperatures equal to the lattice temperature [57]. This means the Hydrodynamic transport approximation is not applicable in this module. On the other hand, the presented device has a non-isothermal domain, therefore the conventional drift diffusion approach should be expanded to consider temperature gradients within the device [71]. To do that, Comsol Multiphysics employs the constitutive drift diffusion equations of electrons & holes are given as, respectively

$$\overrightarrow{J_n} = n\mu_n \nabla E_c + \mu_n k_B T G\left(\frac{n}{N_D}\right)\nabla n + \frac{qn}{T} D_{n,th} \nabla T \tag{2.1}$$

$$\overrightarrow{J_p} = p\mu_p \nabla E_v + \mu_p k_B T G\left(\frac{p}{N_A}\right)\nabla p + \frac{qp}{T} D_{p,th} \nabla T \tag{2.2}$$

where E_c and E_v are conduction and valence band energies, $G(n/N_D)$ and $G(p/N_A)$ is the function representing the degeneracy of the material, $D_{n,th}$ and $D_{p,th}$ are the thermal diffusion coefficients.

For the necessary temperature gradient that is in constitutive drift diffusion equations, the result of the heat transfer in solids module will be used. To calculate this

temperature gradient heat transfer in solids module, the heat generation term outcome of semiconductor module will be employed.

In addition to joule heating, the heat generated by radiative and non-radiative recombination mechanisms in the direct band gap semiconductor materials will be considered in this study. Accordingly, the heat produced in the device is given by

$$q_{ht} = \boldsymbol{E.J} + \left(E_g + 3k_B T\right)R \tag{2.3}$$

where E is the electric field, J is the total current density, E_g, is the bandgap, k_B is the Boltzmann constant and R is the average value of recombination rates of holes and electrons. The first term in Equation (2.3) represents the Joule heating and the second term is recombination heating [66].

Recombination rate is the sum of all recombination mechanisms defined as

$$R_{net} = R_{Aug} + R_{SRH} + R_D, \tag{2.4}$$

where the subscripts represent the net, Auger, Shockley Read Hall, and direct recombination factor respectively.

The Auger recombination rate found using

$$R_{Aug} = (C_n n + C_p p)(np - {n_{i,eff}}^2) \tag{2.5}$$

where $n_{i,eff}$ defined as

$$n_{i,eff} = (\sqrt{N_c N_v})exp\left(-\frac{E_g - \Delta E_g}{2k_B T}\right) \tag{2.6}$$

and np is

$$np = N_c N_v exp\left(-\frac{E_c - E_v}{k_b T}\right). \tag{2.7}$$

In Equations (2.5), (2.6), and (2.7), C_n is the Auger recombination factor for electrons, C_p is the Auger recombination factor for holes, n and p are the intrinsic carrier

concentrations, the effective intrinsic carrier density can be found $n_{i,eff}$, N_c *and* N_v are the effective density of states for conduction band and valence band(Equations (2.11), (2.12), (2.13), and (2.14)), $E_g - \Delta E_g$ is the effective bandgap value after bandgap narrowing, k_B is the Boltzmann's constant.

Shockley read hall recombination rate defined as

$$R_{SRH} = \left(\frac{pn - {n_{i,eff}}^2}{\tau_n(p+p_1)+\tau_p(n+n_1)}\right) \tag{2.8}$$

where n_1, p_1 is

$$n_1, p_1 = n_{i,eff} exp\left(\frac{E_{trap}}{k_b T}\right). \tag{2.9}$$

In Equations (2.8) and (2.9), τ_n and τ_p are the electron and hole carrier lifetimes respectively, E_{trap} is defect energy level with respect to conduction and valence band.

Finally, the direct Recombination rate is defined as

$$R_D = B(np - {n_{i,eff}}^2) \tag{2.10}$$

where B is the Direct (Spontaneous) emission coefficient.

We adopted the recombination parameters from the reference study. Accordingly, in our simulation, the direct recombination coefficient is $2x10^{-11}$, SRH recombination lifetimes are 1 [ns] for electrons and holes through the domain, and Auger recombination coefficient is $1x10^{-34}$.

The density of states of the conduction and valence band of the material layers are calculated as

$$N_c = 2\left(\frac{m_c k_B T}{2\pi\hbar}\right)^{3/2} \tag{2.11}$$

$$N_v = 2\left(\frac{m_v k_B T}{2\pi\hbar}\right)^{3/2}. \tag{2.12}$$

For the quantum wells, the 2D Density of state formulation is being used for electrons given as

$$N_{c,2D} = \frac{k_B T m_c}{\hbar^2 \pi L_z}. \tag{2.13}$$

2D Density of state formulation for holes given as

$$N_{v,2D} = \frac{k_B T m_v}{\hbar^2 \pi L_z} \tag{2.14}$$

where the m_c is effective electron mass in the conduction band, m_v is effective hole mass in valence band k_B is the Boltzmann's constant, and ħ is reduced Planck constant. $L_z$represents the thickness of the quantum well layers. The other required parameters (electron-hole mass) for density of states are calculated based on the method explained by Piprek [85, 86]. The material layers deposited on top of each other create tension/ compression. Under these forces valence bands of the semiconductor tend to split. As a result, hole masses are being accounted differently in such cases. Accordingly, the electron and hole masses for each material layers are calculated by

$$m_v^{3/2} = m_{hh}^{3/2} + m_{lh}^{3/2} \tag{2.15}$$

where m_{hh} represents the heavy hole masses and m_{lh} represents the light hole masses.

In addition, the hole mass of semiconductors differs in transverse and z-direction. We make use of the same reference for calculating the masses in these directions, for the z-direction that LED layers are placed on top of each other, heavy hole and light hole values are calculated with the same equations (see Equations (2.16) and (2.18)). In our structure, the main charge carrier motion occurs in this direction. Accordingly, we calculated effective masses only in z-direction and the values given in Table 2.1 by using the relations

$$m_{hh}^z = -m_0(A_1 + A_3)^{-1} \tag{2.16}$$

$$m_{hh}^t = -m_0(A_2 + A_4 - A_5)^{-1} \tag{2.17}$$

$$m_{lh}^z = -m_0(A_1 + A_3)^{-1} \tag{2.18}$$

$$m_{lh}^{t} = -m_0(A_2 + A_4 + A_5)^{-1}. \quad (2.19)$$

In these equations m_0 represents the unit electron mass. Lastly, the electron masses are calculated by using the linear interpolation by using the effective mass values in the literature [86]. The hole effective mass parameters A_1, A_2, A_3, A_4, A_5 are given in Table 2.1.

Table 2.1. Hole effective mass parameters [86].

	InN	GaN	AlN
A1	-9.24	-7.24	-3.95
A2	-0.6	-0.51	-0.27
A3	8.68	6.73	3.68
A4	-4.34	-3.36	-1.84
A5	-4.32	-3.35	-1.92
m_c	0.11	0.20	0.33

2.1. Model Geometry

We adopted the geometry of the device from the previously conducted work of Piprek *et al.* [73]. Figure 2.1. illustrates the structure of the UV LED simulated with our model which shares the same working principle with visible LEDs. It is fabricated with layers on top of each other respectively: a 3000 nm n-doped GaN, a 100 nm n-doped $In_{0.1}Ga_{0.9}N$, a 1200 nm n-doped $Al_{0.14}Ga_{0.86}N$/GaN Superlattice (SL), a 100 nm n-doped GaN, two layers of 4nm n-$In_{0.15}Ga_{0.85}N$ wells sandwiched between 10 nm n-$In_{0.02}Ga_{0.98}N$ barriers. Over the QW layers, p-doped materials with the given doping concentrations on Table 2.3. are placed on each other respectively: a 20 nm p-doped $Al_{0.2}Ga_{0.80}N$, a 100 nm p-doped GaN, a 600 nm p-doped $Al_{0.14}Ga_{0.86}N$/GaN SL, and lastly a 30 nm p-doped GaN under the p-contact.

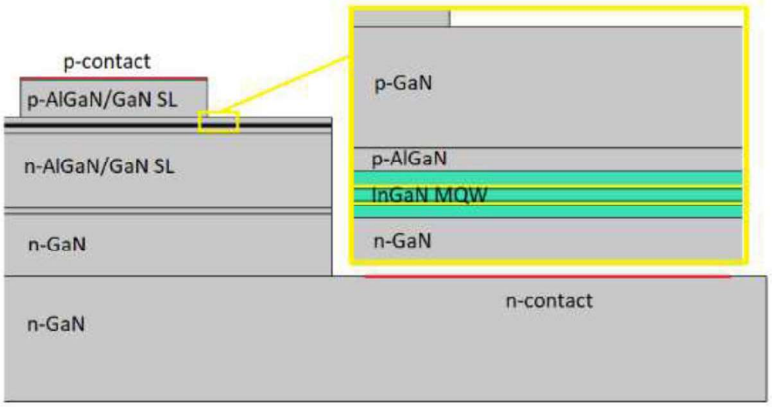

Figure 2.1. Device geometry.

The depth of our device is the same on each layer and is equal to 450 μm similar to the reference device. The structural parameters such as thickness, width, binary material contents, and amount of doping value that we used in our simulation are given in Table 2.2. for each material layer.

Table 2.2. Layer dimensions & contents.

Layer	Thickness [nm]	Width [μm]	Al/In Content [%]	Doping [cm^{-3}]
p-GaN	30	3	0	$2x10^{20}$
p-$Al_{0.14}Ga_{0.86}N$/GaN SL	600	7	0.7	$1x10^{20}$
p-GaN	100	7	0	$5x10^{18}$
p-$Al_{0.2}Ga_{0.8}N$	20	7	0.2	$1x10^{19}$
n-$In_{0.02}Ga_{0.98}N$ Barriers	10	7	0.02	$7x10^{16}$
n-$In_{0.15}Ga_{0.85}N$ QWs	4	7	0.15	$7x10^{16}$
n-GaN	100	7	0	$7x10^{17}$
n-$Al_{0.14}Ga_{0.86}N$/GaN SL	1200	7	0.7	$3x10^{18}$
n-$In_{0.1}Ga_{0.9}N$	100	7	0.1	$3x10^{18}$
n-GaN	3000	14	0	$3x10^{18}$

2.2. Material Parameters

The density of states of Conduction and valence bands and effective messes were calculated by using the stated equations. The Density of states values for 300K domain temperature and effective masses for electrons and holes are given in Table 2.3.

Table 2.3. Conduction band and valence band density of states, electron mass, and hole mass for material layers used in this simulation in 300K.

Layer	Nc [1/m^3]	Nv [1/m^3]	mc [m_0]	mv [m_0]
p-GaN	2.24E+24	1.38E+26	0.2	3.112551
p-$Al_{0.14}Ga_{0.86}N$/GaN SL	2.40E+24	1.45E+26	0.2091	3.218575
p-GaN	2.24E+24	1.38E+26	0.2	3.112551
p-$Al_{0.2}Ga_{0.8}N$	2.70E+24	1.60E+26	0.226	3.435933
n-$In_{0.02}Ga_{0.98}N$	2.21E+24	1.37E+26	0.1982	3.10646
n-$In_{0.15}Ga_{0.85}N$	5.04E+24	8.28E+25	0.1865	3.067442
n-$In_{0.02}Ga_{0.98}N$	2.21E+24	1.37E+26	0.1982	3.10646
n-$In_{0.15}Ga_{0.85}N$	5.04E+24	8.28E+25	0.1865	3.067442
n-$In_{0.02}Ga_{0.98}N$	2.21E+24	1.37E+26	0.1982	3.10646
n-GaN	2.24E+24	1.38E+26	0.2	3.112551
n-$Al_{0.14}Ga_{0.86}N$/GaN SL	2.40E+24	1.45E+26	0.2091	3.218575
n-$In_{0.1}Ga_{0.9}N$	2.09E+24	1.36E+26	0.191	3.082332
n-GaN	2.24E+24	1.38E+26	0.2	3.112551

One of the most fundamental material properties that should be defined for electro-thermal simulation is bandgap energies for each material layers. We calculated the bandgap energies by using the equations

$$E_g\left(Al_xGa_{(1-x)}N\right) = 6.28x + (1-x)3.42 - 1.3x(1-x) \tag{2.20}$$

and

$$E_g\left(In_xGa_{(1-x)}N\right) = 1.89x + (1-x)3.42 - 3.8x(1-x) \tag{2.21}$$

as provided in the literature [73]. Where the x demonstrates the AlN or InN content of the given material layer, the bandgap value of each material is calculated according to these equations are given in Table 2.4. In addition, for each layer 0.6 mEv/K bandgap shrinkage is assumed [73].

Dielectric constant, density, and heat capacity of material layers are calculated by linearly interpolating the binary material parameters using analytical expressions

$$P\left(Al_xGa_{(1-x)}N\right) = xP_{AlN} + (1-x)P_{GaN} \tag{2.22}$$

$$P\left(In_xGa_{(1-x)}N\right) = xP_{InN} + (1-x)P_{GaN} \tag{2.23}$$

given in literature [21]. Superlattice layers are assumed as one bulk ternary material of which composition is the average of components since the total heat generation is not effected [66, 73, 87]. Calculated values of dielectric constant, density, specific heat are presented in Table 2.4.

Table 2.4. Heat capacity, thermal conductivity, bandgap, dielectric constant, and doping concentrations used in the model.

Layer	Heat Capacity [J/kg*K]	Thermal Conductivity [W/cm*K]	Band Gap [eV]	Dielectric Constant [1]	Doping Concentration [1/cm^3]
p-GaN	490	1.3	3.42	9.7	2x10^{20}
p-$Al_{0.14}Ga_{0.86}N$_/GaN SL	497.7	0.2	3.53	9.66	1x10^{20}
p-GaN	490	1.3	3.42	9.7	5x10^{18}
p-$Al_{0.2}Ga_{0.8}N$	512	0.8	3.78	9.58	1x10^{19}
n-$In_{0.02}Ga_{0.98}N$ Barriers	486.6	0.2	3.31	9.8	7x10^{16}
n-$In_{0.15}Ga_{0.85}N$ QWs	464.5	0.2	2.7	10.54	7x10^{16}
n-GaN	486.6	1.3	3.42	9.7	7x10^{16}
n-$Al_{0.14}Ga_{0.86}N$_/GaN SL	464.5	0.2	3.53	9.66	3x10^{18}
n-$In_{0.1}Ga_{0.9}N$	486.6	1.0	2.92	10.26	3x10^{18}
n-Gan	490	1.3	3.42	9.7	3x10^{18}

In our model, we considered both spontaneous polarization and piezoelectric polarization of charges. We used analytical expressions given in the literature to calculate the charge densities applied between material intersections [22]. For the spontaneous polarizations, we used the equations

$$P_{sp}\left(Al_xGa_{(1-x)}N\right) = -0.090x - 0.034(1-x) + 0.021x(1-x) \quad (2.24)$$

$$P_{sp}\left(In_xGa_{(1-x)}N\right) = -0.042x - 0.034(1-x) + 0.037x(1-x). \quad (2.25)$$

The piezoelectric polarization is calculated using

$$P_{pz} = 2 \times \frac{a_s - a_0}{a_0} \times \left(e_{31} - \frac{c_{13}}{c_{33}} e_{33}\right) \quad (2.26)$$

where $e_{xx,}$, a_s and a_0 are piezoelectric constant, lattice constants for substrate and ternary materials respectively. c_{xx} is the elastic constant. Parameters are given in Table 2.5.

Table 2.5. Polarization parameters used in simulation.

Parameter	GaN	AlN	InN
e_{31} [Cm^{-2}]	-0.34	-0.53	-0.41
e_{33} [Cm^{-2}]	0.67	1.5	0.81
c_{13} [GPa]	100	127	94
c_{33} [GPa]	392	382	200
a_0 [Å]	3.189	3.112	3.548

Both polarizations are added together as

$$q \times \sigma_{2D} = P_{sp} + P_{pz} \quad (2.27)$$

to reach net polarization charge densities. It is stated in the reference that real devices experience less than the calculated polarization [73]. Assuming that, 0.2 % of total the calculated polarization of charges applied through the layer intersections as surface charge densities.

In our model, we used incomplete ionization for dopants with overall 200 meV activation energies for acceptors, and 20 meV for donors. It should be noted that, in the reference model, for each layer, the ionization of dopant energies are defined altering by the rate of Al content. However, we assumed an average value for acceptors and donors since otherwise we had to define an additional semiconductor material model in COMSOL semiconductor interface for each layer which is a computationally expensive way.

We calculated the low-field and high field mobilities for each material layer based on the electron transferred mobility model that describes the motion of electrons depending on

the electric field, doping concentration, and temperature [19, 20]. The temperature dependence and doping dependence of the mobility are given as

$$\mu_0(T,N) = \frac{\mu_{min}\left(\frac{T}{300}\right)^{\beta_1} + (\mu_{min} - \mu_{max})\left(\frac{T}{300}\right)^{\beta_2}}{1 + a_1\left(\frac{N}{N_{ref}\left(\frac{T}{300}\right)^{\beta_3}}\right)^{\alpha_1\left(\frac{T}{300}\right)^{\beta_4}}}. \quad (2.28)$$

The electrical field dependence of the mobility is given as

$$\mu(T,N,E) = \frac{\mu_0(T,N) + v_{sat}\frac{E^{n1-1}}{Ec^{n1}}}{1 + a\left(\frac{E}{Ec}\right)^{n2} + \left(\frac{E}{Ec}\right)^{n1}}. \quad (2.29)$$

Constants used in these equations are given in Table 2.6. Mobility parameters N_{ref}, β_1, β_2, β_3, β_4, α, n1, and n2 are adopted from given references. To fit the IV curve, we changed the v_{sat} and E_c values.

Table 2.6. Mobility parameters for binary material layers.

Properties	GaN	AlN	InN
N_{erd} [cm^{-3}]	1.00E+17	1.00E+17	1.00E+17
β_1	-1.02	-1.82	-6.39
β_2	-3.84	-3.43	-1.81
β_3	3.02	3.78	8.05
β_4	0.81	0.86	-0.94
a_1	0.66	1.16	0.68
v_{sat} [cm/s]	1.91E+09	2.17E+07	2.04E+09
E_c [V/m]	6.16E+05	6.16E+05	5.24E+04
n_1	7.2044	17.3681	3.8501
n_2	0.7857	0.8554	0.6078
a	6.1973	8.7253	2.2623

For heat transfer modeling, thermal conductivity and specific heat are required. The temperature dependence of these parameters has been widely investigated by several researchers [88–90]. Figure 2.2. demonstrates the variation of heat capacity of GaN, the main material that our device is made up of, with temperature respectively. The thermal conductivity of semiconductor materials decreases with temperature. Conversely, the heat capacity increases, as illustrated. Even though these changes seem opposite, while the lattice temperature increases both of the properties change in a way of increasing the heat

retention capability of the system. Therefore, we expect to see these parameters effective on temperature distribution in a high-power device.

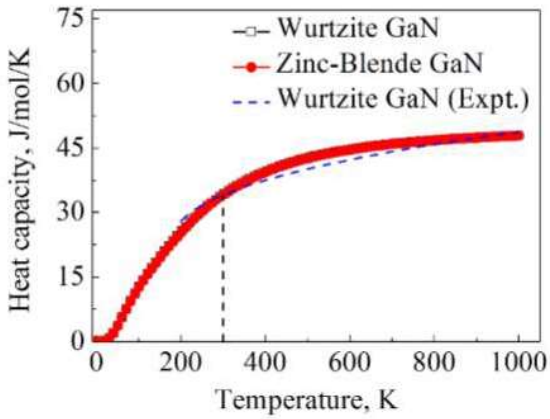

Figure 2.2. Temperature dependent heat capacity of GaN obtained from theoretical calculation (dashed line) and experimental study from literature [88].

In the literature, most of the electrothermal studies neglect the temperature dependent characteristics of these parameters. In our work, we will demonstrate the importance of temperature dependence of thermal parameters. For thermal conductivity, we used the general power law mobility model given in Equation (2.30) that has been used by many studies to approximate the change in bulk conductivity values with altering temperature [91, 92]:

$$k(T) = k_{300}\left(\frac{T}{300}\right)^{\alpha_k} \tag{2.30}$$

where k_{300} represents the thermal conductivity of bulk material at 300K environmental conditions. α_k constants vary depending on doping density [93], Al fraction [94], and thickness of material [95]. Here, we extracted the α_k values for binary materials from literature, then interpolated them for ternary material parameters. For GaN 0.45 [91, 96], for AlN 1.7 [97], for InN 0.1 [98] are selected. For specific heat, we used the proposed temperature dependence formulation by Palankovski *et. al.* [92] that is defined as

$$c_L(T) = c_{300} + c_1 \frac{\left(\frac{T_L}{300K}\right)^{\beta} - 1}{\left(\frac{T_L}{300K}\right)^{\beta} + \frac{c_1}{c_{300}}}. \quad (2.31)$$

In the equation, c_{300}, the specific heat at 300K value is taken as the previously shared constant heat capacities. β and c_1 constants are directly adopted from the same study.

2.3. Mesh structure

Our model consists of a mapped mesh with shrinking element distribution introduced in the vertical direction. For each layer, from the middle to the borders, the element sizes decrease to ensure finer elements between layer intersections and electrical contacts. For the n-GaN layer, this shrinkage is employed only from the bottom to n-pad direction to clearly see the possible current crowding regions. This mesh type is selected for a faster simulation. We constructed the mesh with the minimum element size of 0.1 [µm] in the lateral direction and 0.001 [nm] in the vertical direction. Mesh structure for a coarser element selection is illustrated in Figure 2.4. for better visualization.

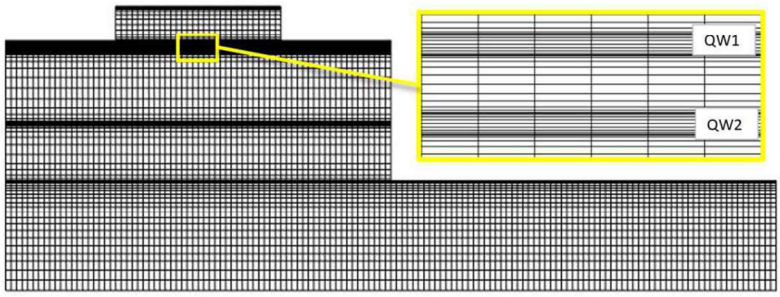

Figure 2.3 Magnified mesh structure.

2.4. Study details

COMSOL semiconductor module can be coupled with heat transfer module however equations are not solved simultaneously. To be able to run an electro thermal study firstly an initial state which is defined as the equilibrium study is conducted. In this study, the fermi levels are assumed to be constant through all material layers, in case of no applied voltage, and all the domain is assumed at 300K. From the calculated charge distribution, a secondary voltage sweep study is conducted. For voltage sweep study, the base

temperature is assumed to change depending on the power of the device that is analytically calculated by the thermal resistance method.

A third study is conducted as fully coupled. According to this study a cyclic relation is defined. According to this relation, at each iteration step heat generation profile of the result of the semiconductor module is applied to the heat transfer module.

2.5. Model Validation

The first step for this study is model validation. To validate our model for each case, we followed three steps. Firstly, we matched the band diagram of the conduction band of the reference device, then we also matched the IV curve to assure the similar characteristics our device shows with the reference. Lastly, we applied a mesh refinement to assure the mesh quality.

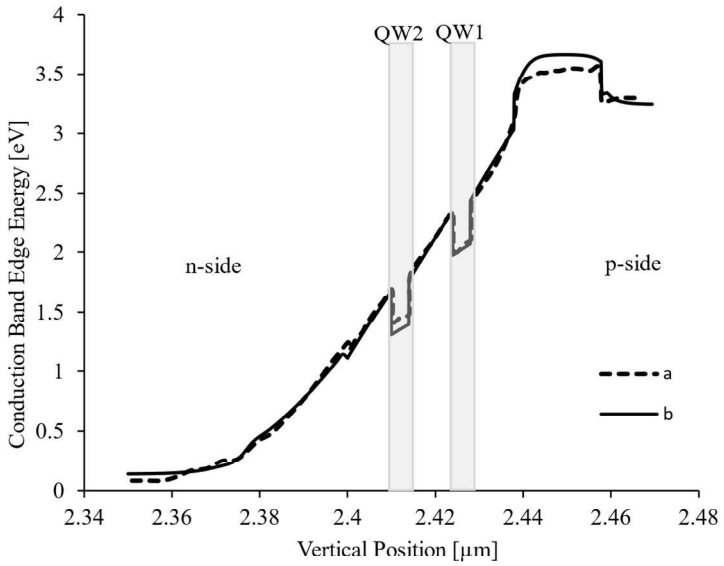

Figure 2.4. Conduction band energies of electro-thermal models (a) Piprek *et al.* [73], (b) this study.

In Figure 2.5., the conduction band edge energy of our 2D model is compared with the reference study. The values for Figure 2.5. and 2.6. are extracted by digitizing the graphs from the study of Piprek *et. al.* [73].

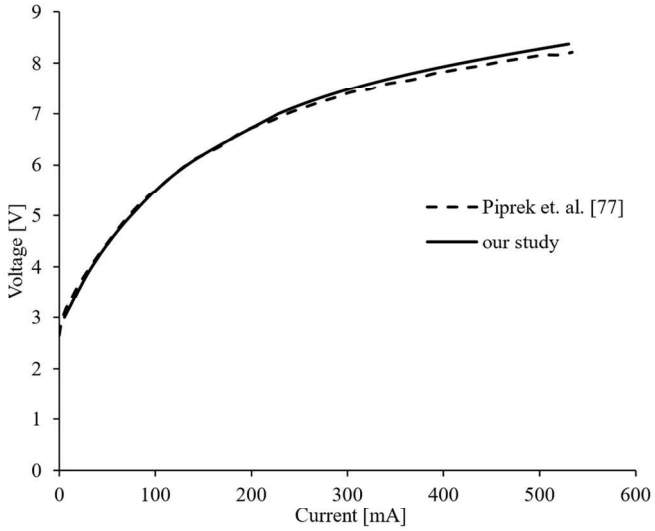

Figure 2.5. IV curve matching.

In Figure 2.6 characteristic IV curve of both studies is given. According to this graph, we can assure that our electro thermal model approximates the reference device model well.

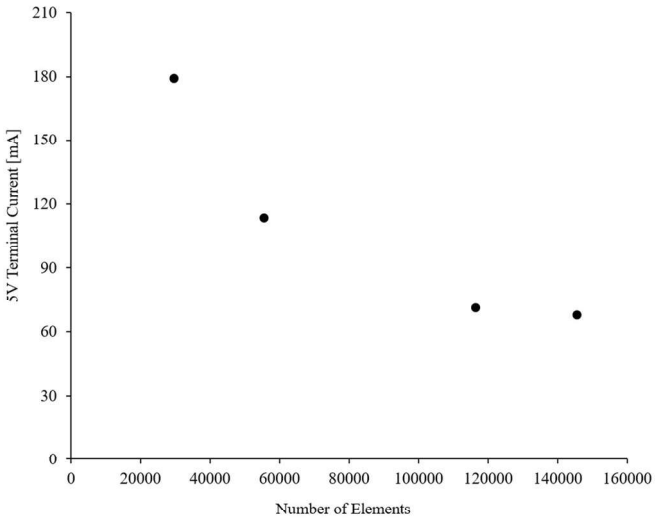

Figure 2.6. Mesh quality study.

We ensured the quality of the mesh structure by repeating the simulation for finer element sizes. In our last two studies, the number of mesh elements increased ten times, but the change of terminal current with the same simulation setup at 5V was less than 0.045 %. That is an acceptable result for our study.

The constant domain temperature studies are used in literature for quicker and easy to converge simulations. In these studies, the heat diffusion equations are not being used or the device domain is assumed to be at a constant 300K. All the parameters were used for their 300K values. To observe whether this assumption can be used in a high current operation, we employed a constant isothermal study that both the domain and boundary kept in 300K with and without the thermal diffusion equation. In Figure 2.8. the resulting IV curve of these studies is presented. This study reveals the importance of conducting a fully coupled study. After reaching 5V, the temperature of the device increases, and the temperature dependent electrical parameters become important actors of device behavior. At higher voltages, even though in the fully coupled study we assumed a perfect cooling of the device by room temperature boundary condition, device VI curves differ a lot. This means, non-coupled studies may lead to wrong results including computing wrong heat generation in high injection current applications. As a result, we employed electro-thermal models for the following chapters.

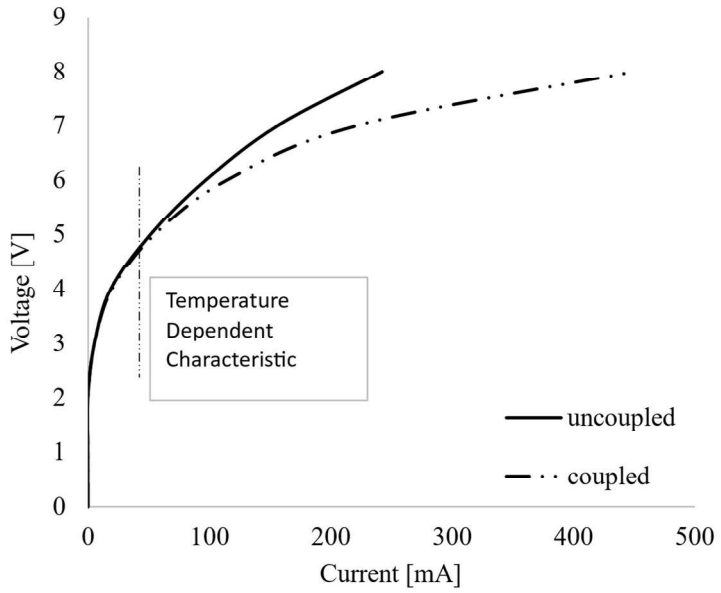

Figure 2.7. IV curves from coupled & uncoupled simulations.

2.6. Conclusion

To be able to simulate the real device behavior, it is important to match the IV curve of the model to the IV curve of the real device. Because the total heat generation

at an operating power is directly related to the injection current and voltage of the subjected device. In addition, the refinement level of the mesh is one of the main steps of model validation to assure each necessary point in the domain is being accounted for in the calculations. We could successfully reach similar behavior for both validation checks. Moreover, we also matched the reference model band energy diagram with the current model to assure selecting the correct material parameters for modeling.

3. LOW TEMPERATURE STUDY

In this chapter, we investigated the thermal behavior of the LED while exposed to perfect heat removal. This case will be an indicator of hotspot formation without the effect of interactions with other chips in the array.

3.1. Boundary Conditions

Electrical and thermal boundary conditions are being set as follows. For the electrical simulation, we assumed that all structure is positioned over an insulating substrate which results in lateral electrode placement. This creates lateral current in addition to the strong vertical charge movement. As presented in the upper shape of Figure 2.9 with blue borders, all the structure is assumed to be surrounded by electrically insulated surface except p-contact and n- contact regions that are the electrodes themselves.

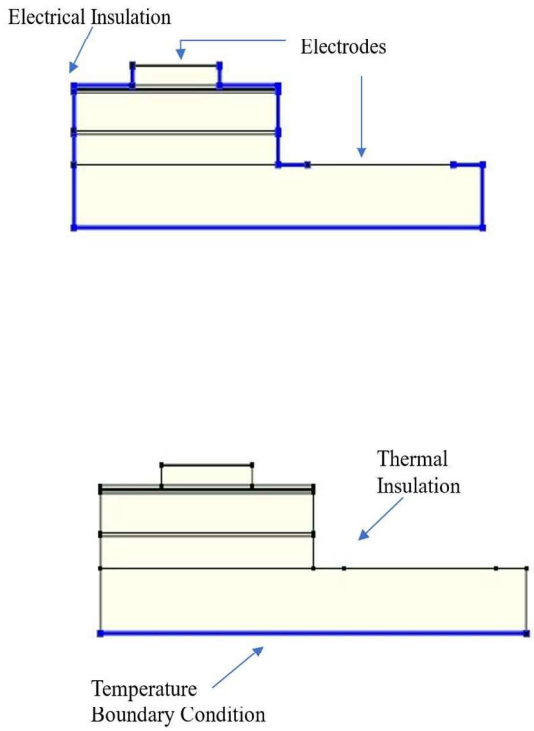

Figure 3.1. Electrical and thermal boundary conditions of LED device electro-thermal model.

We assumed that the base temperature of the chip is maintained at the 300K temperature boundary condition (see Figure 2.8) to assure the perfect heat removal.

3.2. Results

The resulting temperature profile of the device as an outcome of our simulation is presented in Figure 3.2. We see the localization of temperature on the middle of the quantum well region and ridge under the p-contact. Although generated heat is assumed to be removed perfectly, the temperature distribution inside the junction area varies 10 K from the middle to mesa edges.

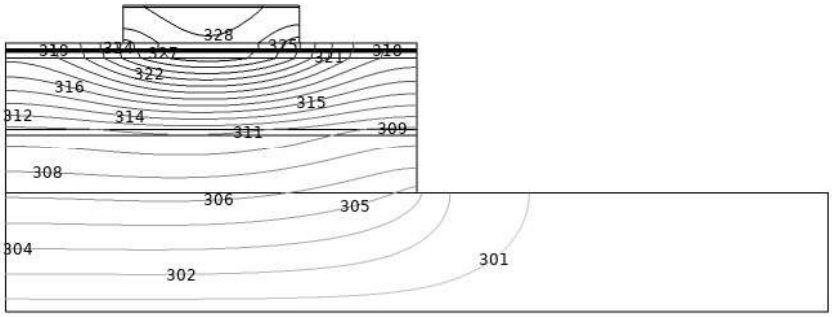

Figure 3.2. Temperature distribution of LED operating at 7V.

Even though localization of heat generation is an expected phenomenon at high current operated devices, in complex geometries such as in this example, accurate determination of maximum temperature regions is difficult. In the literate given in section 1, there are many studies presented to identify the effective parameters that cause localization of heat. Obeying the common view, we expect to see current crowding and localization of self-heating at the right edge of the mesa around the quantum well region since our device is a high-power lateral device. However, the resulting temperature distribution is more like a vertical device. Therefore, we can deduce by making such coarse approximations, we may apply improper heat generation conditions in thermal studies. On the other hand, the distribution of temperature depends on not only the heat generation term but also other parameters such as thermal conductivity and boundary conditions. For this reason, we will further examine the thermal and electrical behavior of the device.

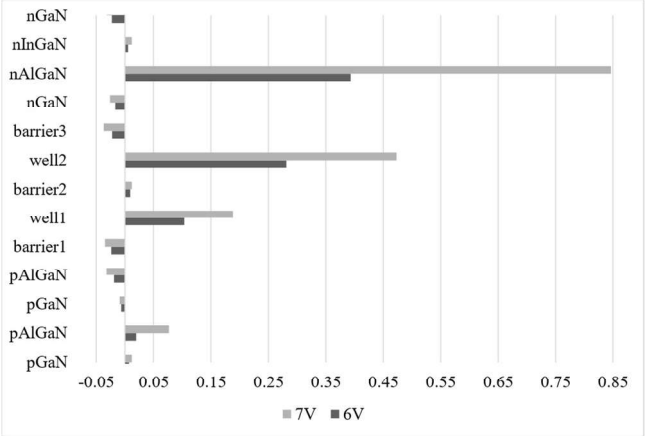

Figure 3.3. Total heat generation of device layers for 6V and 7V.

To examine the heat generation, the total heat generation of the device layers are plotted individually and compared the amount of heat generation at 6V and 7V operating conditions. At first sight, in Figure 3.3., the negative heat powers generated at some layers can be noticed due to the thermoelectric Thomson effect. However, it is too weak to be the dominant force. On the other hand, the maximum heat generations were observed in n-AlGaN, first and second quantum wells. We should note that again, the graph provides the total heat generation of all volumes of layers. If the heat generation per total volume of these layers (i.e., heat generation density) are considered, it can be viewed that even though the largest heat generation occurs in the n-AlGaN layer, this region does not expose to the highest temperatures. Since its dimensions are quite big compared to quantum wells which only have 4nm thickness. So that, the total volumetric heat generation in quantum wells is much higher than in other layers. In addition, on the p-AlGaN layer, the device geometry has a ridge that has a half width of the mesa. Although the heat generation is fairly small in this region, the effective area is also small and surrounded by heat generation and insulating boundaries. As a result, high temperatures are observed in this region. However, other effects and behavior of the device will be examined to further understand the heating mechanism.

The volumetric total heat generation through the upper edge nodes of the second quantum well (QW2) on the lateral direction for four altering operation conditions is investigated to observe temperature distribution since this region is exposed to the highest heat generation. From the Figure 3.4. the heat generation in the lateral direction looks

uniform at low operation conditions. Non-uniformity of heat generation grows with the increase of operating power as expected. Increasing operating voltage has a boosting effect on heat generation. Similar to stated information in the literature, increasing injection current density may be the reason for this localization.

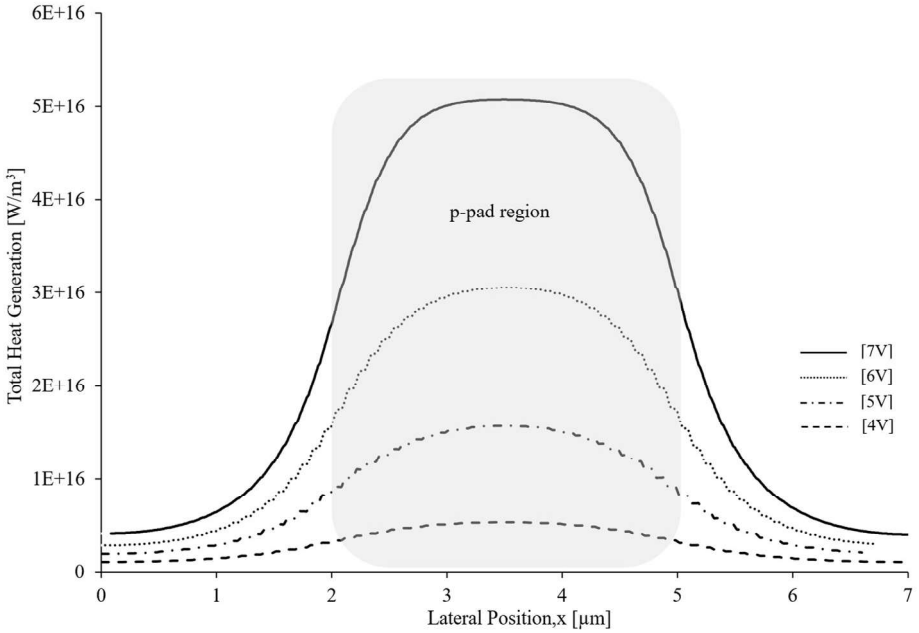

Figure 3.4. Total heat generation for 7V, 6V, 5V and 4V applied voltage operation conditions.

The 2D temperature profiles of this device for 4V, 6V, and 7V powers also provided in Table 3.1. To make a comparison between the literature and our work, additionally, 2D current density distribution plots are provided in the same table. Our aim is to set a relationship between the possible current crowding regions and heat generation. Focusing on the 4V and 7V powers, at 7V, even though the device doesn't reach the maximum power yet in the given operating conditions, localization of current density draws attention. From the literature, current density localizes around the shortest path resistance through the p and n contacts where generally the places with sharp edges. However, again contrary to our expectations, even though at lower operation powers the temperature distribution is more uniform, the regions of high current density do not coincide with the regions of high temperature. It may be because of the AlGaN current blocking layer which reduces the effect of current crowding.

Table 3.1. Temperature distribution vs current density distribution.

[V]	Temperature Distribution [K]	Current Density Distribution [A/m^2]
4V	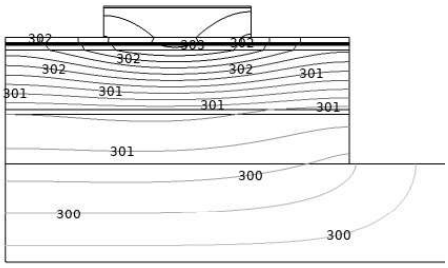	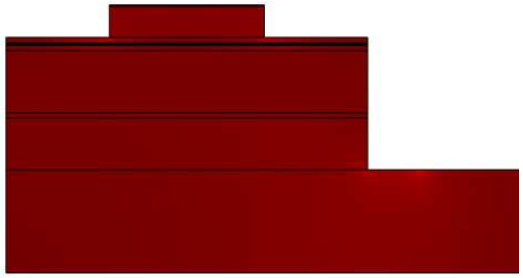
5V	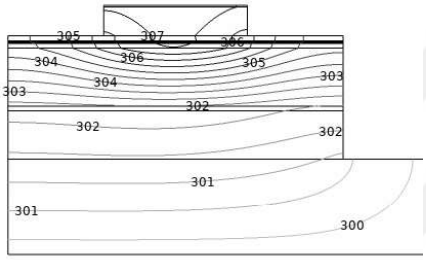	
6V	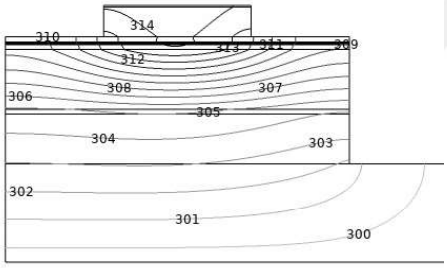	
7V	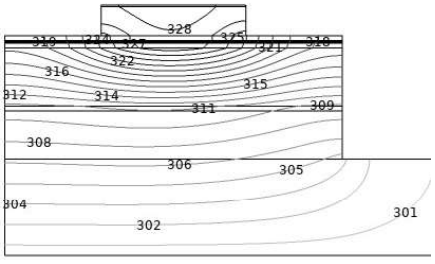	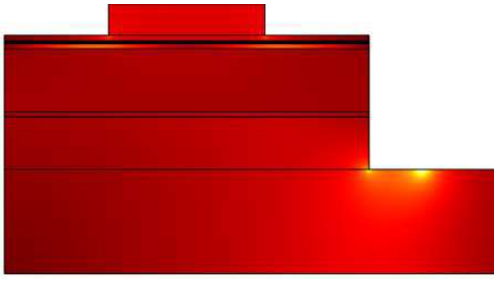

On the other hand, the selected device has a high current density operating condition that injection current density over 100 mA which leads to observe the current crowding effects. Therefore, the heat generation and related phenomena are further investigated in the following steps.

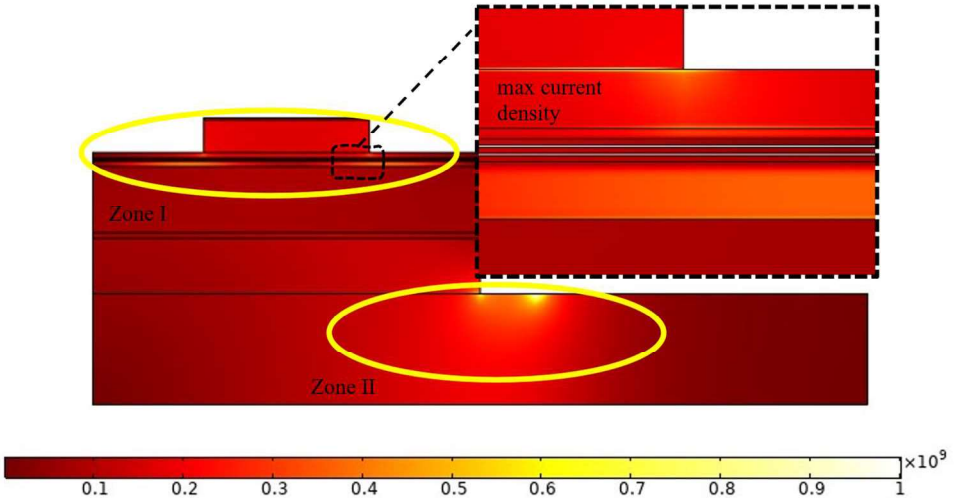

Figure 3.5. Current density distribution (highest regions are indicated by yellow rings).

In Figure 3.5. the total current density 2D plot for 7V is presented. In the figure, the current density is localized below the ridge, on the mesa corner, and around the left edge of the n-contact. Since the emerging of current crowding is visible in the lateral direction, two high current density regions as zone I and zone II are marked for the investigation in Figure 3.4. Current density reaches its maximum value in the zone I and zone II that are the areas in and around the quantum well regions below the corners of ridge geometry respectively.

Based on this situation, it is concluded that either the local heating effects in the device are minimized with the existing excellent cooling or that these effects are not important in the thermal behavior of this device. However, before a final judgment, all heat generation mechanisms must be checked. As stated in the first chapter, heat generation due to current crowding is called joule heating. To observe the relation between heat generation from Joule heating and current density distribution, we plotted the current density and volumetric joule heating in the lateral direction at the edge of 2nd QW in Figure 3.6. The results were in line with our predictions. Current density and joule heating occur in parallel, but this does not explain the total heat generation profile.

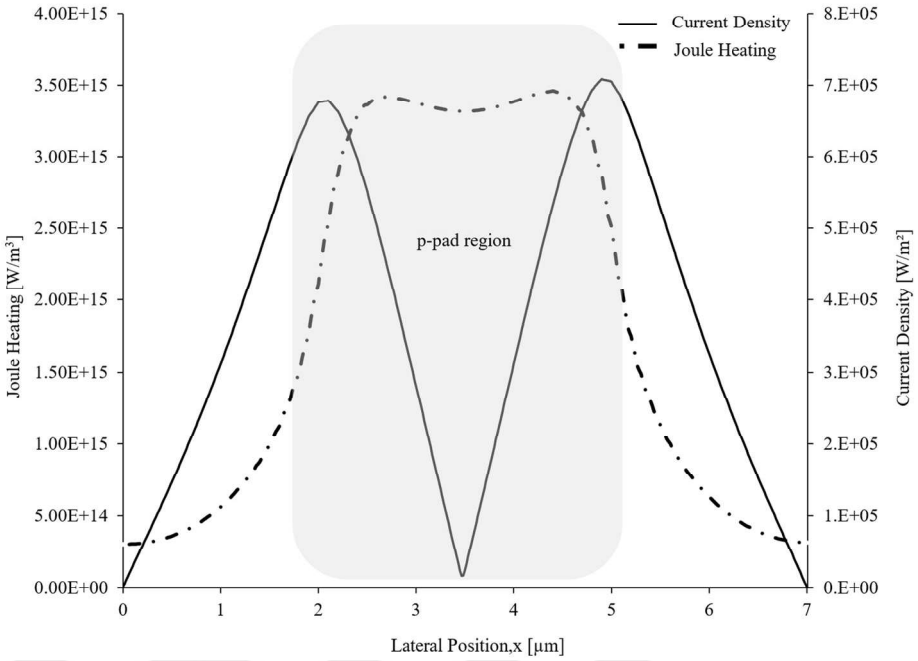

Figure 3.6. Current density and joule heating on the edge of the second QW at 7V operating condition.

Next, we compared the non-radiative recombination and joule heating in Figure 3.7. at zone I on the edge of QW2 in the lateral direction. From the figure, the difference between the magnitude of the recombination heating and joule heating is quite large. This indicates that recombination heating is the dominant heating mechanism in the zone I. As a result, the temperature profile reflects the recombination heating profile, not the joule heating!

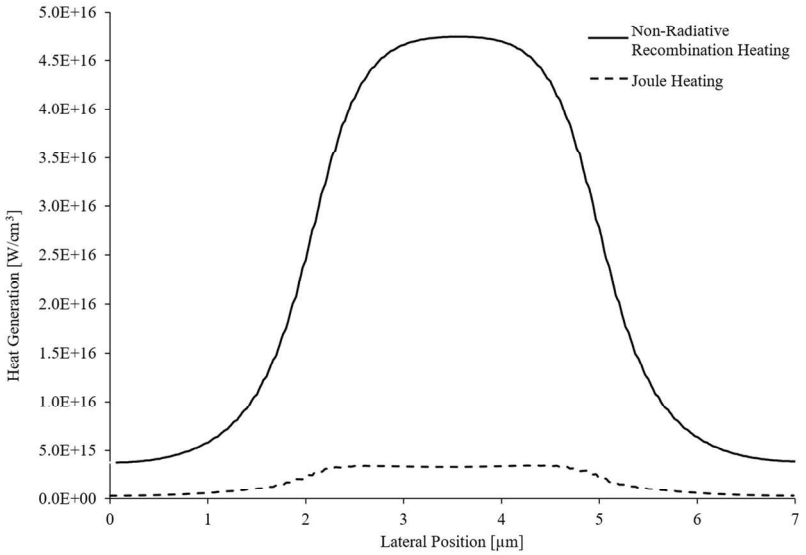

Figure 3.7. Recombination and joule heating at the edge of second QW at 7V operating condition.

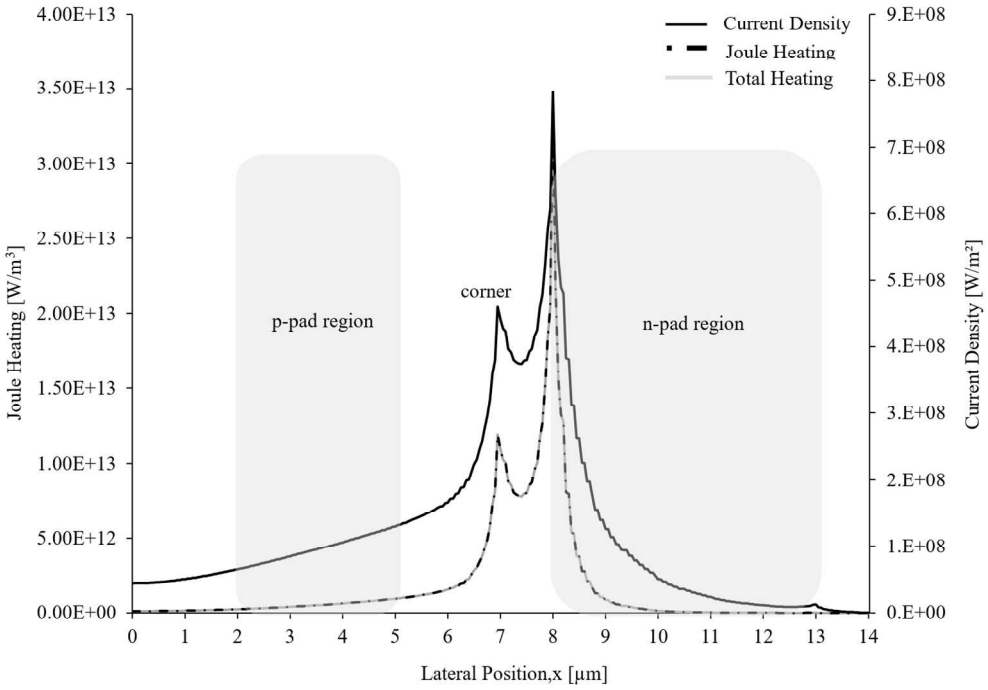

Figure 3.8. Current density, joule heating and total volumetric heat generation in zone II.

Secondly, zone II is investigated with the same aspect. In this region, see in Figure 3.8., contrary to zone I, the total heat generation is parallel to the current density distribution. Since there is no recombination occurs in this region, the contribution of non-

radiative recombination heating to total heat generation value is very weak. As a result, the amount of total heat is generated due to joule heating and reflects the current density distribution profile. On the other hand, although local heat generation is observed in this region, we cannot see the hotspot temperatures at the same points at the temperature maps given in previous figures. It is concluded that the heat generation is either suppressed by the advanced cooling very close to this region or bulk material conductivity is big enough the dissipate the generated heat from the region.

3.3. Discussion

3.3.1. Thermal approach vs Electro-Thermal studies

As mentioned in previous sections, there are other methods that are easy to implement and quick to solve compared to massive electro-thermal simulations. The ability of these methods to the accurate prediction of device thermal behavior is questioned. In this section, the comparison of the results of simulations that are employed uniform and non-uniform heat generations through the domain case. In the thermal approach, the total heat generation is assumed to occur uniformly in the domain. Replicating the highly applied method, this uniform heat generation term is applied to all domains in the heat transfer module. In Figure 3.9. resulting temperature maps at 7V obtained by electro-thermal fully coupled and thermal studies are presented. The Figure on the left side represents the electro-thermal simulation results considering the nonuniform heat generation case, while the figure on the right-hand side represents the thermal simulation with uniform heat generation. The thermal study predicts the maximum temperatures around the same regions with electro-thermal simulation. However, it lower estimates the maximum temperature values. The thermal simulation case gives a non-realistic temperature distribution. On contrary, electro thermal non-uniform case gives localized regions. While working with thermal simulations, an error coefficient should be used to eliminate poor estimation. However, we may further infer from these results, that if the localization was around the mesa edge and was mainly because of Joule heating, the result of thermal simulation would lead to less promising results.

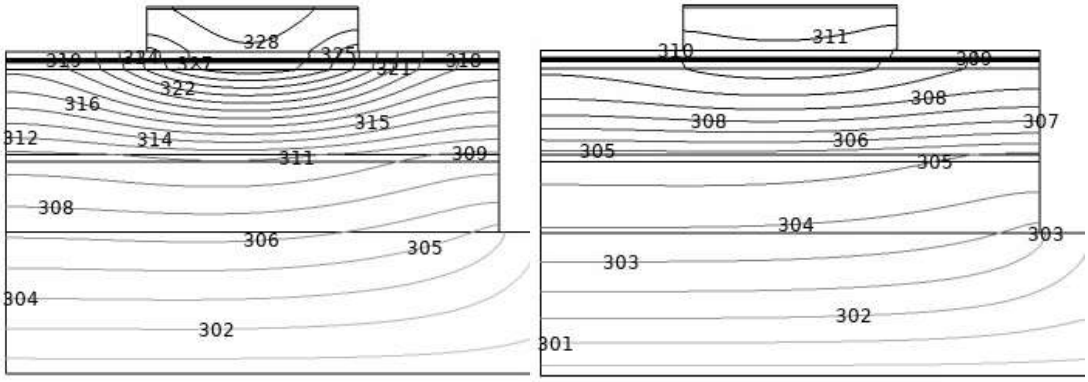

Figure 3.9. Temperature maps for (a) non-uniform heat generation, b) uniform heat generation applied on entire geometry.

Moreover, the results of resistive, uniform heat generation, and electro thermal models for altering operation powers are compared in Table 3.2. It is observed that for low operation powers all the three methods give similar results. However, while the operation power increases there is a strict divergence between the results of different approaches. It is obvious for high power operations Electro-thermal models give more promising results.

Table 3.2. Quantum well region maximum temperatures calculated by three different methods.

Voltage [V]	Total Heat Generation [W]	Tj from Resistive Approach	Tj from Electro thermal Model	Tj from Diffusion approach
4V	0.112	301	302	301
5V	0.32	302.5	306	302
6V	0.706	305.7	314	305
7V	1.45	311.76	328	311

3.3.2. Temperature Dependent Thermal Conductivity and Specific Heat

Many of the electro thermal studies include the temperature dependent properties in the model. However, most of them neglect the temperature dependency of thermal conductivity and heat capacity. On the other hand, these parameters play a significant role in heat dissipation. To reveal the necessity of using these parameters, in this section we employed a study to compare both cases.

Table 3.3. Temperature maps of comparison study for temperature dependent thermal conductivity effect.

V	Temperature dependent thermal conductivity used simulation	Constant thermal conductivity and specific heat used simulation
8V	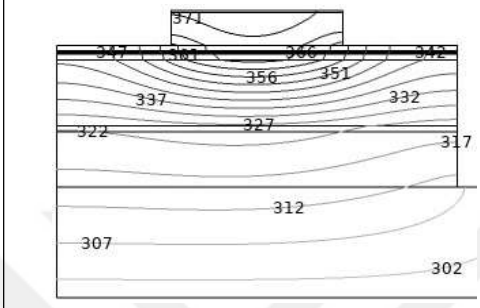	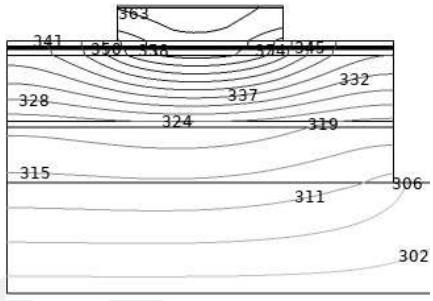
7V	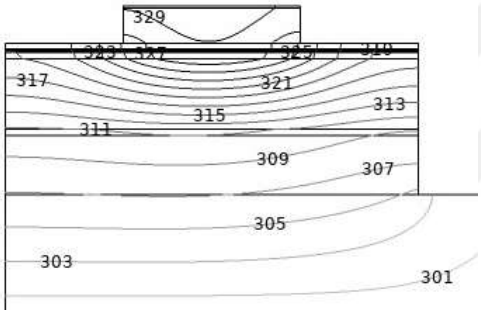	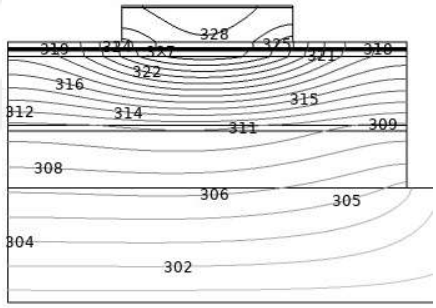
6V	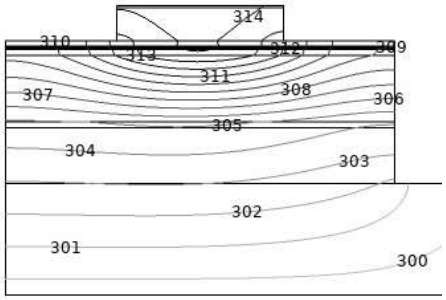	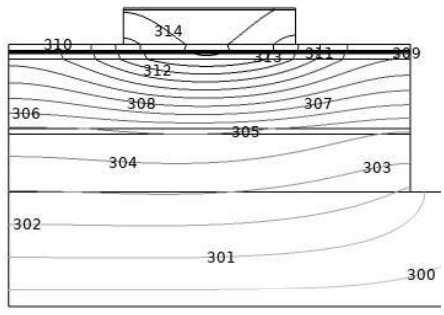

In Table 3.3. the temperature maps of 8V,7V, and 6V operating powers demonstrated that simulated by employing temperature dependent and constant thermal conductivities. Interestingly, at 6V power using a temperature dependent conductivity does not affect the dissipation of heat. It may be because 314K is a low temperature to make a difference in the magnitude of thermal conductivity. Similarly, the result of the 7V operation only changes 1 K by using a temperature dependent thermal conductivity. However, when the operation power increases to 8V, the maximum temperature of the device increases, and also the difference between the two results rises. It can be inferred that for many LED

applications, using temperature dependent conductivity only increases the complexity of the model while giving the exact same temperature distribution with the constant thermal conductivity used ones. However, the high-power applications where device temperature is high, it is important to consider the decrease in the thermal conductivity with altering temperature.

Next step of the study, the effect of temperature dependent heat capacity on the temperature distribution of the device is investigated. Electro-thermal simulations for constant-and temperature dependent conductivity cases are employed. The resulting temperature distributions are presented in Table 3.4. This time we see no change on temperature maps of two cases till the device operating voltage reaches to 8V. Moreover, at the highest operating power, temperature dependent heat capacity only makes a 3K difference on maximum temperatures. So, we can infer that for the material combinations used in this device, the temperature dependence of heat capacity may be neglected. However, it seems clear that the effect of thermal dependence of these parameters should be reconsidered at high temperature applications since we observed that the effect of using temperature dependent parameters shows up more vividly at higher powers.

From the thermal diffusion equation presented in previous sections, lowering the thermal conductivity while increasing the specific heat affects the domain in a way to increase the maximum temperatures. On the comparison studies for each parameter, the temperature increasing effect becomes stronger at high powers. However, these studies are performed to understand each effective parameter individually. Next step of this investigation, a simulation is performed by considering the temperature dependence of both thermal conductivity and specific heat. In future discussions, this study will be called as the mixed study. The results are presented in Table 3.5.

In the previous comparison for 6V, there was no difference between the temperature-dependent conductivity and heat capacity, and the simulation results with the unbound. In both cases, the resulting temperature profile was the same. For mixed simulation, we obtained the same result which indicates that for low temperatures no need for using temperature dependent formulation.

Table 3.4. Temperature maps for constant and temperature dependent specific heat.

V	Temperature dependent specific heat	Constant thermal conductivity and specific heat
8V	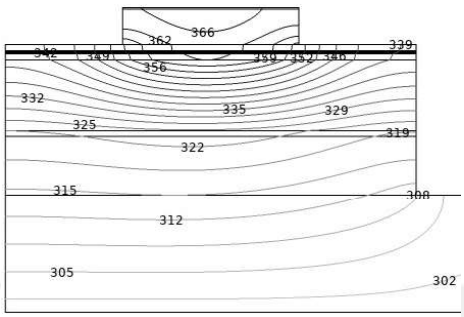	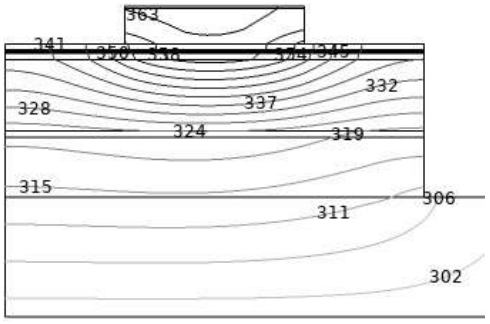
7V	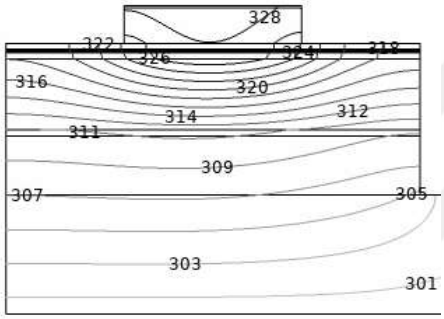	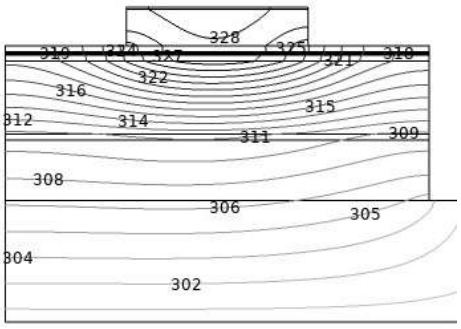
6V	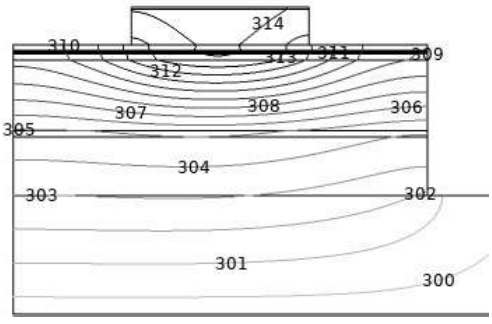	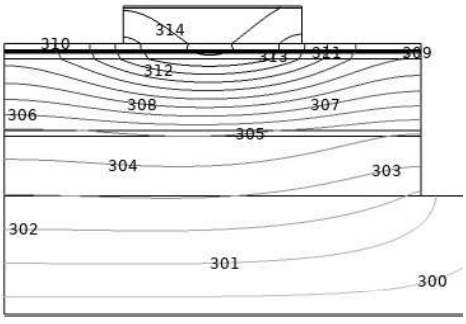

In Table 3.5., the resemblance between the study of only temperature dependent thermal conductivity simulation and mixed simulation is prominent. For 7V and 8V, the resulting temperature maps are exactly the same for both studies. This is also indicating that thermal conductivity is the dominant parameter for heat diffusion.

Table 3.5. Temperature maps for mixed model and constant thermal parameters.

V	Temperature dependent thermal conductivity and specific heat	Constant thermal conductivity and specific heat
8V	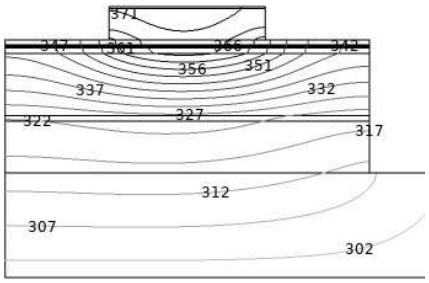	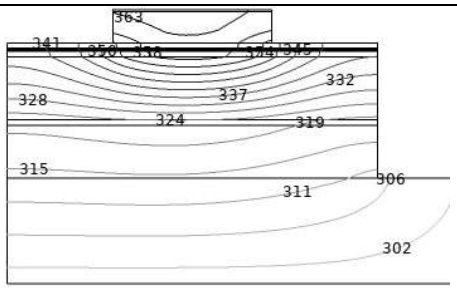
7V	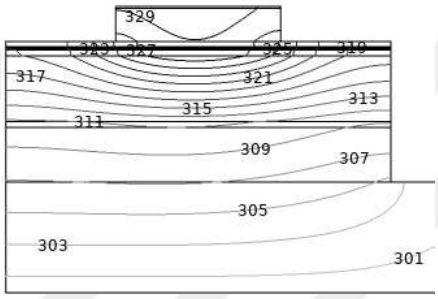	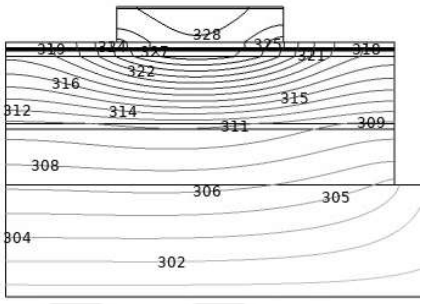
6V	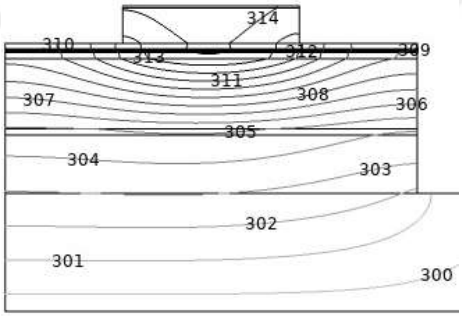	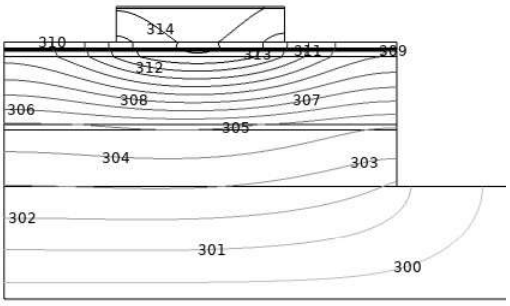

3.4. Conclusion

Even though the device is maintained at 300K base temperature which indicates a perfect cooling, formation of high current density and temperature regions are observed. The localization of temperature on the middle of the quantum well region and ridge under the p-contact is obvious. However, the high current density regions do not coincide with the high temperature regions due to dominant heat generation mechanism non-radiative recombination. Formation of current crowding on the mesa corner and left point of n-contact do not have a profound effect on temperature distribution.

The thermal resistance approach may lead inaccurate calculation of junction temperatures for high power applications since at high temperatures it lower estimates the temperatures.

Temperature dependency of thermal conductivity and specific heat may be neglected for low power approximations since the temperatures values can not reach to a value that the effect of these parameters can be felt strongly.

4. HIGH TEMPERATURE STUDY

At this part of the study, a more realistic case that the LED is mounted on a heat sink that has a resistance value larger than 0 is investigated. Of course, the usage of LEDs on different applications brings a variety of boundary conditions that must be considered while modeling the thermal behavior. An LED might be mounted on a heat sink as in our example or on a Peltier cooler, or on an electric board that is exposed to an active cooling by a fan. However, for lighting applications, the most widely used applications are the heat sinks. Even though the heat sinks are designed to remove the heat from the device, they are not capable of providing the perfect cooling conditions as in the previous chapter because of their own thermal resistance. As a result, LED boundary temperatures are much higher than the ambient temperature. Here for the high temperature study, we will use a thermal resistance assuming if there is a heat sink below the n-GaN.

4.1. Boundary Conditions

Electrical boundary conditions are the same as the ones in the previous chapter. The thermal boundary condition is applied to the same surface with a different value. An estimated value of 30 K/W thermal resistance boundary condition value is provided by a previous reference study. For thermal simulation, differently from their application, we assigned a surface temperature under the n-GaN layer (base) that was derived based on the IV curve of the real device and thermal resistance of the heat sink. To calculate the appropriate temperature boundary condition for each operation power the analytical thermal resistance method is used. The thermal resistance was estimated as 30 K/W for the heat sink. Since there is no electrical operation ongoing in the heat sink and since it has macroscopic dimensions, we assumed the environmental temperature as 300K and calculated the base temperature by using the power of each operating condition. More specifically, by multiplying the injection current and operating voltage of the device, we found total power. Then, we assumed that at high injection currents the efficiency of the device is about % 0.2. So, we reached the total heat power. By using the thermal resistance method, we calculated the base temperature. To be able to use this boundary condition in our electro-thermal simulation, we make a curve fit by OriginPro to build up a relation

between İnjection current and voltage. By using this equation, we lastly formulated the altering base temperature of the real device as

$$T = 0.8 \times \left(-0.02564 + 0.02564\, exp\left(\left(\frac{V-2.65306}{1.78297}\right)V\right)\right) \times 30\ \left[\frac{K}{W}\right] + 300[K]. \quad (4.1.)$$

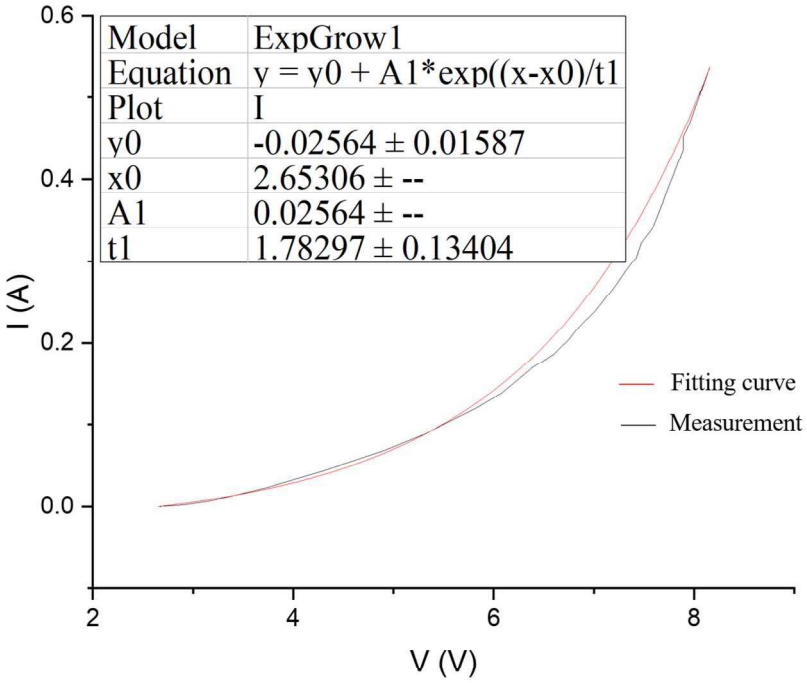

Figure 4.1. The fitting curve and IV curve of the device, fitting curve equation in the box.

In these new chapter studies, only the bottom boundary condition has changed. According to the new environmental condition, the IV curve was rematched with new mobility values following the same steps presented in chapter 2. Accordingly, the heat generation mechanism and thermal behavior were investigated.

4.2. Results

The temperature distribution profile of the device as an outcome of our high temperature study is presented in Figure 4.2. For 6V. Even though the temperature of the device increases significantly, resulting in temperature distribution through the quantum wells is more uniform. In low temperature study, the difference in temperatures of the

middle and edges of the quantum wells in lateral direction was 5K, while in the high temperature study we obtained 3K. Localization of temperature on the middle of the quantum well region and ridge under the p contact.

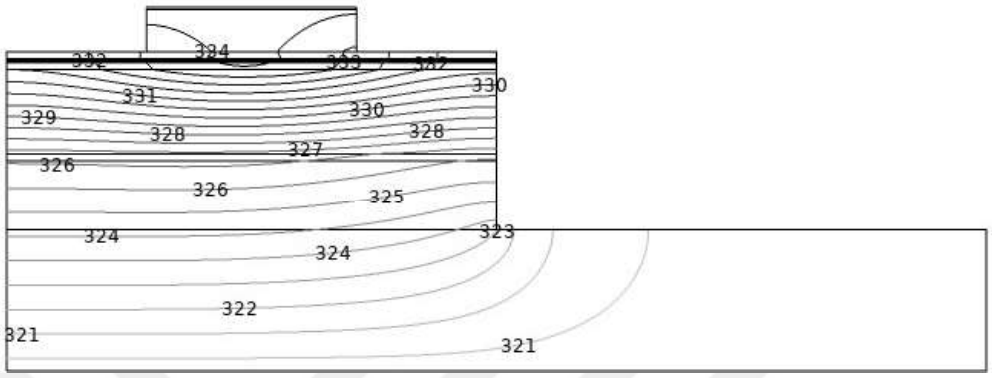

Figure 4.2. The temperature distribution map for high temperature study at 6V.

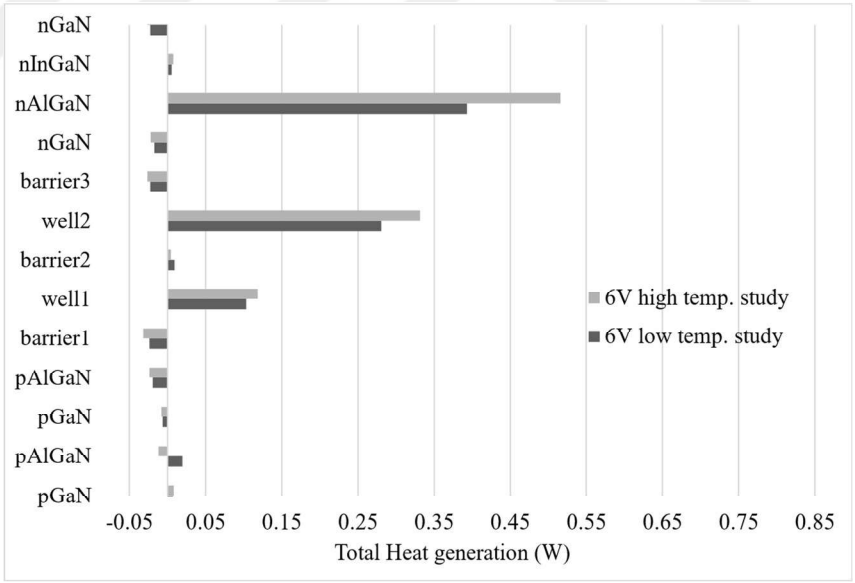

Figure 4.3. Total heat generation of device layers for 6V high temperature and low temperature studies.

In Figure 4.3. the total heat generation of device layers for high and low temperature studies presented. From the graph, heat generation inside the material layers is much higher than the low temperature study results. Since the heat generation is directly related to the electrical operating parameters, we can emphasize the statement in the literature that

temperature increase affects the performance of the device, in other words, the temperature profile and the boundary conditions are effective on device behavior.

Table 4.1. Comparison of temperature maps of high and low temperature cases for 5V and 6V.

6V low temperature study	6V high temperature study
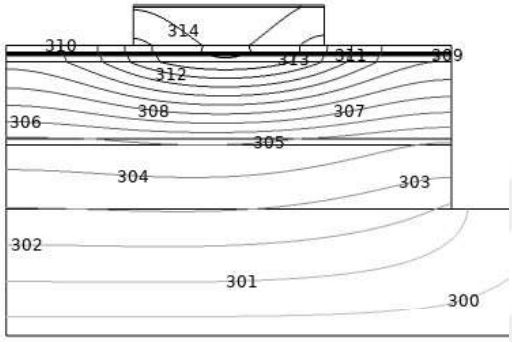	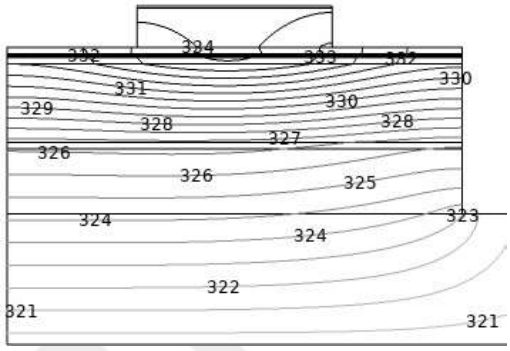
5V low temperature study	5V high temperature study
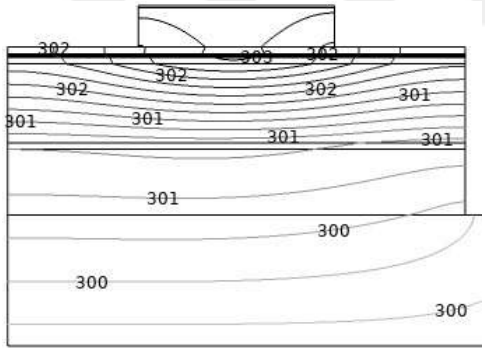	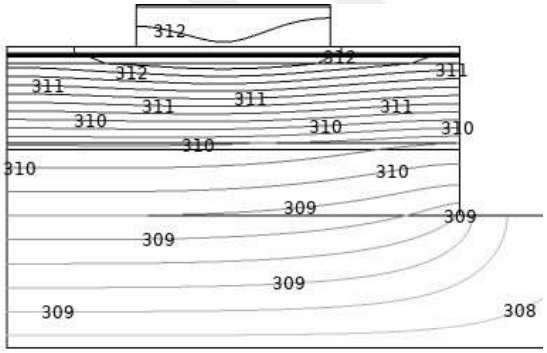

For comparison of both cases, temperature maps for 5V and 6V operating powers for low temperature and high temperature studies are presented in Table 4.1. For further examine the thermal behavior of high and low studies, the current density maps for 5V and 6V compared with the ones in low temperature study at the same powers. From the given current density maps on Table 4.2., we can see that the locations of high current density regions do not change abruptly. Indeed, for the 5V power current density distributions, the magnitude is also quite similar. However, if we focus on the zone I area of 6V power, we can observe the decrease in current density at the high power study. Conversely, the zone II region looks brighter than the low temperature study. This situation might indicate the

increase in current crowding by high power operations. To clearly address the phenomenon, similar to the presented ones in chapter 3, we plotted the heat generations in the lateral direction for zone I and zone II regions.

Table 4.2. Comparison of current density maps of high and low temperature cases for 5V and 6V.

6V high temperature study current density distribution [A/m2]	6V low temperature study current density distribution [A/m2]
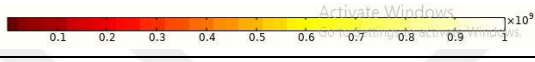	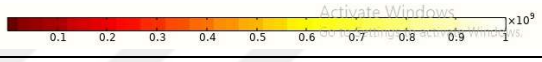
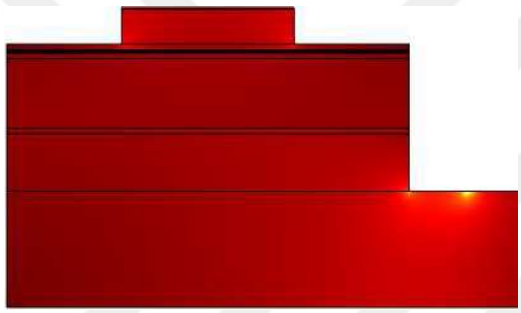	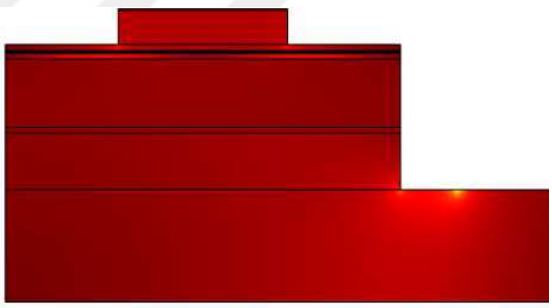
5V high temperature study	5V low temperature study
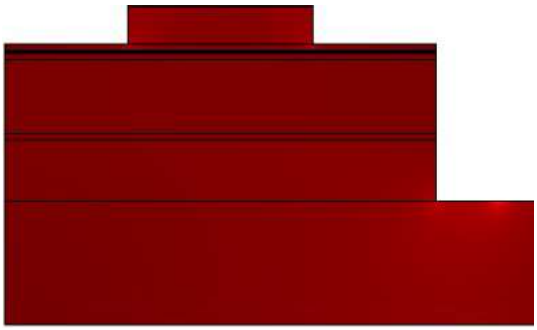	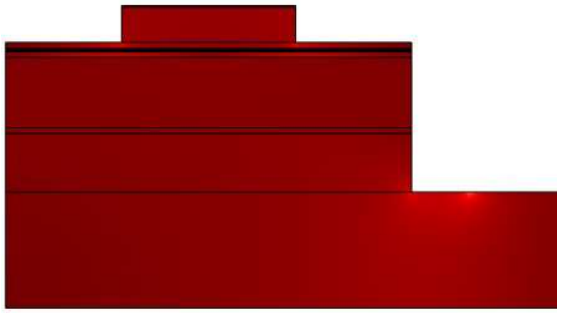

The total heat generation at 6V on the edge of the second quantum well is presented in Figure 4.4. at the middle of the quantum well region, where a high rate of non-radiative recombination heating occurs, the heat generation decreases at high temperature study. This is an unexpected result since at higher temperatures the efficiency of the device decreases which means the amount of energy converted to the self-heating should be increased.

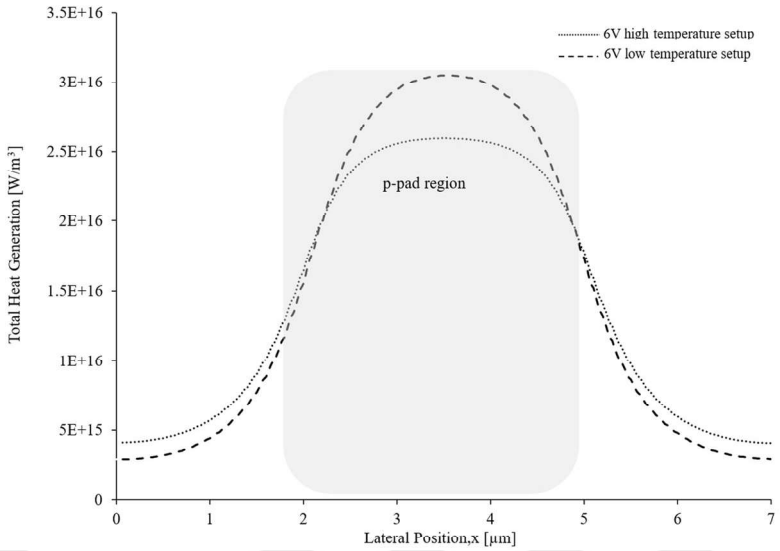

Figure 4.4. Total heat generation through the edge of second quantum well.

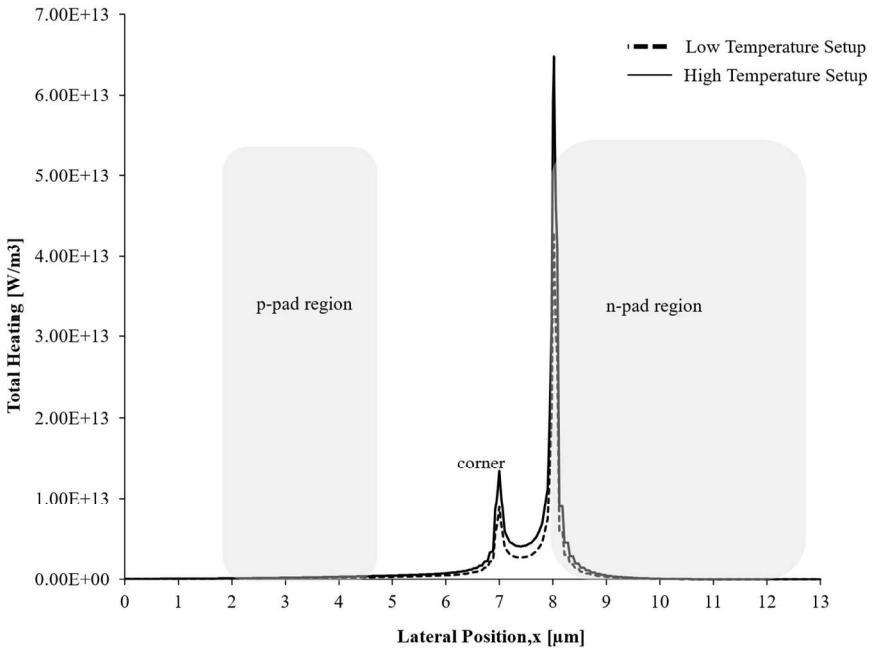

Figure 4.5. Heat generation on the zone II for with heat sink and without heat sink condition.

Secondly, plotted the heat generation in zone II at 6V is presented in Figure 4.5. The figure directly illustrates the migration of heat generation to the regions that high current

density is observed. If we look closely at two sharp peaks, which show the location of the very left of the n-pad and mesa corner, the increase in joule heating is obvious.

4.3. Discussion

4.3.1. Thermal approach vs Electro-Thermal studies

Similar to what we did in chapter three, at high temperature study case we examined the thermal model results in comparison with the electro thermal results. Similar to our previous findings, we observed that the thermal model lower estimates the maximum device temperatures.

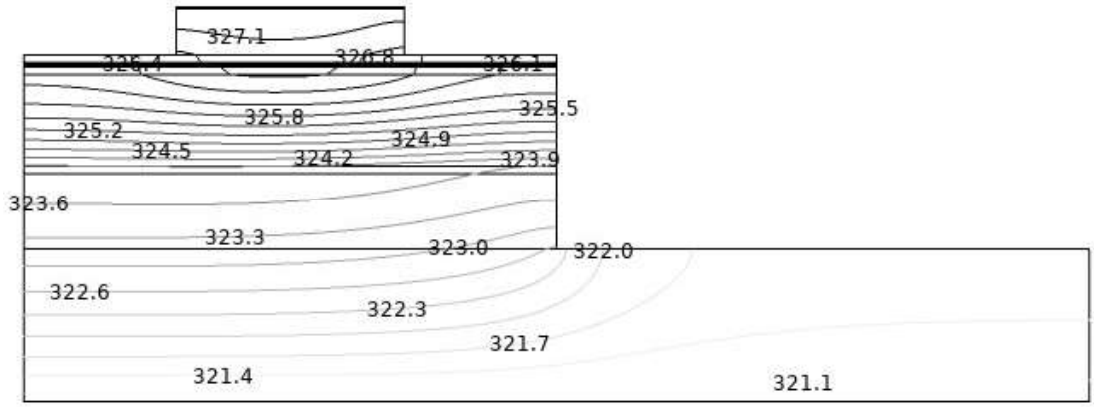

Figure 4.6. Uniform heat generation thermal model for high power study.

4.3.2. Temperature Dependent Thermal Conductivity and Specific Heat

From the low temperature study results, our expectation is that at high power conditions the temperature dependency of the thermal conductivity and heat capacity would be stronger. For this case, the device reaches higher temperatures at lower operating powers. For example, while for low temperature study the domain reaches approximately 30K maximum temperature at 7V, for the high temperature case we see that at 6V. To clearly understand the difference, we took the same temperature domains for investigation in Table 4.3. The situation is similar to the low temperature study, around 30K temperatures the difference between the two models is only 1 K while at lower domain temperatures it is insignificant. From these two studies, we can deduce that if the domain is

exposed to high temperatures, the temperature dependency of thermal parameters becomes important.

Table 4.3. Comparison of the effect of temperature dependence of thermal parameters.

6 V high temperature study constant thermal conductivity and specific heat case	6 V high temperature study temperature dependent thermal conductivity and specific heat case
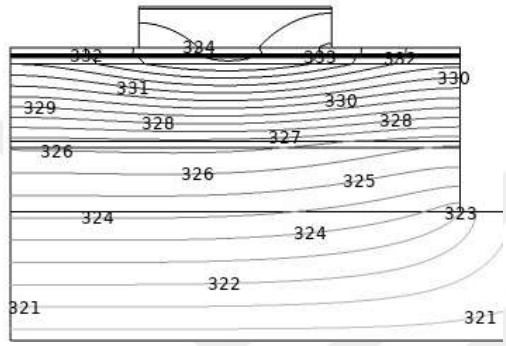	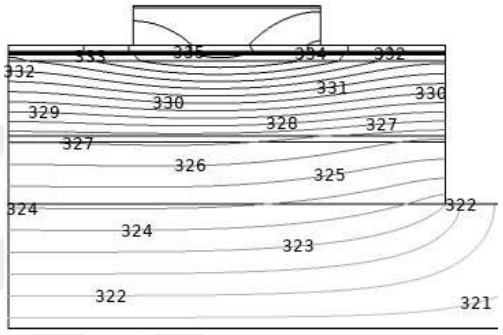
5V high temperature study constant thermal conductivity and specific heat case	5V high temperature study temperature dependent thermal conductivity and specific heat case
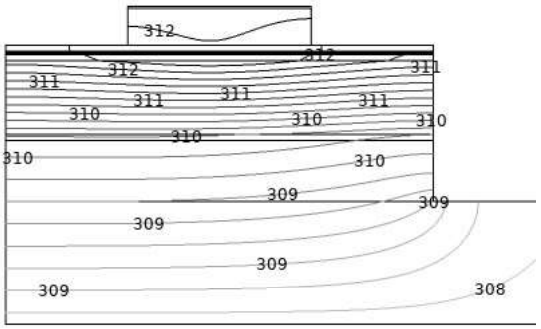	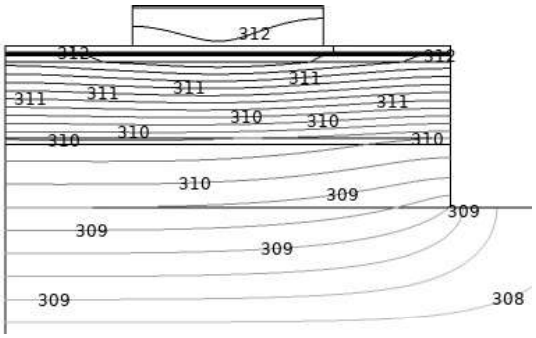

4.4. Conclusion

In this chapter, the boundary temperature is altered at each operating power based on the IV curve. Heat generation inside the material layers is found higher than the low temperature study results for the same operating power indicating that temperature affects the performance of the device.

There is no difference on the formation points of maximum temperature and current crowding regions compare to the low temperature study. However, high temperature study shows that increasing boundary temperature leads joule heating to increase. As a result, has an increasing effect on current crowding. It is deduced that the boundary conditions are highly effective at junction temperature determination.

The thermal resistance approach failed to simulate the device behavior appropriately also at high temperature study.

Lastly, for the high temperature setup the effect of the temperature dependence of thermal conductivity and heat capacity is much higher compared to low temperature, indicating that the effect might further increase at higher operation temperatures.

5. CONCLUSION & FUTURE STUDIES

We demonstrated the electrical and thermal behavior of a UV LED by employing a 2D electro-thermal simulation in the Comsol Semiconductor Module. The non-uniform heat generation, local heating, and temperature distribution mechanism of the device is investigated by utilizing several simulation setups. The two main heat generation term and their magnitudes in lateral and vertical directions are examined. Results are also compared with electrical phenomenon current crowding to enlighten the effect of it on thermal behavior. We validated our results by comparing the characteristic IV curve and conduction band energy diagram of the real device that is available in the literature.

Contrary to mostly studied lateral LED's, we observed that for this device temperature hot spots are not placed on the mesa edge or under the p and n contacts. The maximum temperatures are seen on the ridge and middle of the quantum well regions. We deduced that it is mainly because of high volumetric non-radiative heat generation in the middle of the quantum wells and insulated boundary layers surrounding these regions. Therefore, a general assumption of expecting hot spot regions in and around the high current density regions is not a correct assumption always. Therefore, applying total heat generation from the upper surface, quantum well, or from the bottom of the device may lead to wrong results although these are widely used methods in the literature.

Thermal simulations applied with uniform heat generation and thermal resistance approaches underestimate the maximum temperatures in both high and low temperature set ups. Thermal simulations should employ an error coefficient to eliminate the error. However, at each operating power, the difference between these models is quite different. Therefore, at each power, the total heat generation should be increased at a certain amount rate before applying to the model to obtain similar results with the electro thermal simulations. On the other hand, even though for this device is a must but more studies are needed to accurate determination of this constant. On the other hand, even if the high temperature points are overlapped for this study, the thermal model will not make the right approximation in the case of a device with the joule heating is dominant heating

mechanism. In order to confirm this statement, similar comparison studies should be conducted on a device where temperatures are determined according to joule heating.

Thermal boundary conditions also play a significant role in device temperature distribution. Insulating boundary conditions were applied to the weak heat flux with natural convection on those tiny surfaces. This boundary condition removes no heat from the device so that the only heat removing boundary remains the n-GaN base. On low temperature study, effective removal of heat from this boundary creates excellent cooling in the device. Therefore, on the left side of the n-contact temperature increase is limited. Moreover, current density on the left-hand side of the n contact is weaker compared to the region under the ridge, as a result, it can easily be removed and has almost no effect on device temperature. However, at the high temperature study, an increase in joule heating is observed. İt may further increase and become a dominant heat source. Therefore, in future studies, the effect of joule heating at higher powers for this device should be investigated to make a final statement.

Lastly, the effect of the temperature dependence of thermal conductivity and heat capacity on device thermal behavior has been investigated. Simulation results show that for low domain temperatures, low power applications, temperature dependency of thermal conductivity and heat capacity should be neglected for a less complex model. On the other hand, for high power applications, neglecting these dependencies may lead to wrong junction temperature estimations even though the electro thermal studies employed.

REFERENCES

1. The National Academies of Sciences, Engineering, and Medicine, *Energy Efficiency, Lighting*, 2012, http://needtoknow.nas.edu/energy/energy-efficiency/lighting/, accessed in January 2022.

2. U.S. Energy Information Administration (EIA), *Frequently Asked Questions (FAQs)*, 2021, https://www.eia.gov/tools/faqs/faq.php?id=99&t=3, accessed in December 2021.

3. Department of Energy, *LED Lighting*, 2021, https://www.energy.gov/energysaver/save-electricity-and-fuel/lighting-choices-save-you-money/led-lighting, accessed in January 2022.

4. Holonyak, N. and S. F. Bevacqua, "Coherent (visible) Light Emission from $Ga(As_{1-x}P_x)$ Junctions", *Applied Physics Letters*, vol. 1, no. 4, pp. 82–83, 1962.

5. Nakamura, S., T. Mukai, and M. Senoh, "Candela-Class High-Brightness InGaN /AlGaN Double-Heterostructure Blue-Light-Emitting Diodes", *Applied Physics Letters*, vol. 64, no. 13, p. 1687, 1998.

6. Al-Amri, M. D., M. M. El-Gomati, and M. S. Zubairy, *Optics in Our Time*, Springer Nature, Cham, 2016.

7. Piprek, J., T. M. Katona, S.P. DenBaars, and S. Li, "3D Simulation and Analysis of AlGaN/GaN Ultraviolet Light-Emitting Diodes", *Light-Emitting Diodes: Research, Manufacturing, and Applications VIII*, vol. 5366, p. 127, 2004.

8. Mukai, T., M. Yamada, and S. Nakamura, "InGaN-based UV/blue/green/amber LEDs", *Integrated Optoelectronic Devices*, vol. 3621, pp. 2–13, 1999.

9. Neumark, G. F., I. L. Kuskovsky, and H. Jiang, *Wide Bandgap Light Emitting Materials and Devices.,* Wiley, Darmstadt, 2007.

10. Sun, X., D. Li, H. Song, Y. Chen, J. Hong, G. Miao, and Z. Li., "Short-Wavelength Light Beam in Situ Monitoring Growth of InGaN/GaN Green LEDs by MOCVD", *Nanoscale Research Letters*, vol. 7, p. 282, 2012.

11. Epperlein, P. W., *Semiconductor Laser Engineering, Reliability and Diagnostics: A Practical Approach to High Power and Single Mode Devices*, Wiley, West Sussex, 2013.

12. Pierret, R. F., *Semiconductor Device Fundamentals*, Addison-Wasley Publishing, New York, 1996.

13. Pierret, R. F., *Advanced Semiconductor Fundamentals*, Second Edition, Prentice Hall, Indiana, 1987.

14. Schubert, E. F., *Light-Emitting Diodes*, Second Edition, Cambridge University Press, Cambridge, 2006.

15. Neamen, D. A., *Semiconductor Physics and Devices*, Third Edition, McGraw Hill, New York, 2006.

16. Mottier, P., *LEDs for Lighting Applications*, Wiley, London, 2010.

17. Ye, H., S. Koh, C. A. Yuan, and G. Q. Zhang, "Thermal Analysis of Phosphor in High Brightness LED", *Electronic Packaging Technology and High Density Packaging 13th International Conference 2012 Proceedings*, Guilin, China, 13-16 August 2012, pp. 1535–1539, IEEE, 2012.

18. Bogdanov, M. V., K. A. Bulashevich, O. V. Khokhlev, I. Y. Evstratov, M. S. Ramm, and S. Y. Karpov, "Current Crowding Effect on Light Extraction Efficiency of Thin-Film LEDs", *Solid State Physics.,* vol. 7, no. 7–8, pp. 2124–2126, 2010.

19. Ni, X., X. Li, H. Liu, and N. Izyumskaya, "On the Light Emission in GaN Based Heterostructures at High Injection", *Materials Research Society Symposium Proceedings*, vol. 1202, pp. 159–167, 2010.

20. Hao, G. D., M. Taniguchi, N. Tamari, and S. I. Inoue, "Enhanced Wall-plug Efficiency in AlGaN-Based Deep-Ultraviolet Light-Emitting Diodes with Uniform Current Spreading p-Electrode Structures", *Journal of Physics D Applied Physics*, vol. 49, no. 23, 2016.

21. Li, C. K. and Y.R. Wu, "Study on the Current Spreading Effect and Light Extraction Enhancement of Vertical GaN/InGaN LEDs", *IEEE Transactions on Electron Devices*, vol. 59, no. 2, pp. 400-407, 2012.

22. Piprek, J., Ha*ndbook of Optoelectronic Device Modeling and Simulation: Fundamentals, Materials, Nanostructures, LEDs, and Amplifiers*, CRC Press, Taylor & Francis Group, FL, 2017.

23. Othman, M. F., S. Ahmad, F. N. A. Saad, A. N. Alias, A. A. Aziz, and M. R. Hashim, "Current Crowding Effect in Lateral and Vertical LED Configurations: 3D Simulation and Characterization", *2012 IEEE International Conference on Control System, Computing and Engineering*, Penang, Malaysia, 23-25 November 2012, pp. 530–534, IEEE, 2012.

24. Bi, W. W., H. C. H. Kuo, P. C. Ku, and B. Shen, *Handbook of GaN Semiconductor Materials and Devices,* CRC Press, Taylor & Francis Group, FL, 2017.

25. Guo, X. and E. F. Schubert, “Current Crowding and Optical Saturation Effects in GaInN/GaN Light-Emitting Diodes Grown on Insulating Substrates”, *Applied Physics Letters,* vol. 78, p. 3337, 2001.

26. Robidas, D., S. Singh, S. Pal, and C. Dhanavantri, “Study of Current Crowding Effect in Different Led Die Structures”, *Optoelectronics and Advanced Materials-Rapid Communications*, vol. 4, no. 10, pp. 1461–1464, 2010.

27. Kim, H., S. J. Park, and H. Hwang, “Effects of Current Spreading on the Performance of GaN-Based Light-Emitting Diodes”, *IEEE Transactions on Electron Devices*, vol. 48, no. 6, pp. 1065–1069, 2001.

28. Li, C. K., Y. R. Wu, and J. Singh, “Modeling of Junction Temperature and Current Flow in High Power InGaN/GaN Light Emission Diodes Using Finite Element Methods”, *13th International Workshop on Computational Electronics*, Beijing, China, 27-29 May 2009, pp. 1–4, IEEE, 2009.

29. Kumar, S., S. Singh, A. K. Lunia, S. Pal, and C. Dhanavantri, “Optimization of n-Electrode Pattern for p-Side Down Vertical InGaN/GaN Blue Light Emitting Diodes”, *Solid State Physics*, vol. 211, no. 9, pp. 2134–2141, 2014.

30. Sato-Iwanaga, J., Y. Liu, R. W. Dutton, H. Tsuchiya, and T. Yokogawa, “Theoretical Considerations on Efficiency Degradation due to Thermal Effect in a Planar GaN-Based LED with a GaN Substrate*”, Japanese Journal of Applied Physics,* vol. 53, no. 10, 2014.

31. Roibu, A., R. B. Morthala, M.E. Leblebici, D. Koziej, T. Van Gerven, and S. Kuhn, “Design and Characterization of Visible-Light LED Sources for Microstructured Photoreactors”, *Reaction Chemistry and Engineering*, vol. 3, no. 6, pp. 849–865, 2018.

32. Abdelmlek, K. B., Z. Araoud, K. Abderrazek, K. Charrada, and G. Zissis, “Effect of Deficient Thermal Grease on the Junction Temperature of LEDs Package”, *2015 COMSOL Conference in Grenoble*, Grenoble, France, 14-16 October 2015, pp. 3–5, Comsol, 2015.

33. Luo, X., T. Cheng, W. Xiong, Z. Gan, and S. Liu, “Thermal Analysis of an 80W Light-Emitting Diode Street Lamp”, *IET Optoelectronics*, pp. 191–196, 2007.

34. Wu, B., Luo X., and Liu S., “Effect Mechanism of Moisture Diffusion on LED Reliability”, *3rd Electronics System Integration Technology Conference*, Berlin, Germany, 13-16 September 2010, pp. 1-5, IEEE, 2010.

35. Arik, M., K. S. Kulkarni, C. Royce, and S. Weaver, “Developing a Standard Measurement and Calculation Procedure for High Brightness LED Junction Temperature”, *Fourteenth Intersociety Conference on Thermal and Thermomechanical Phenomena in Electronic Systems*, Orlando, USA, 27-30 May 2014, pp. 170–177, IEEE, 2014.

36. Xi, Y., J.Q. Xi, T. Gessmann, J. M. Shah, J. K. Kim, and E. F. Schubert, “Junction and Carrier Temperature Measurements in Deep-Ultraviolet Light-Emitting Diodes Using Three Different Methods”, *Applied Physics Letters*, vol 86, no.3, p. 031907-9, 2005.

37. Xi, Y., T. Gessmann, J. Xi, and J.K. Kim, “Junction Temperature in Ultraviolet Light-Emitting Diodes”, *Japanese Journal of Applied Physics*, vol. 44, no. 10, pp. 7260–7266, 2005.

38. Zhong, C., Z. Jihong, S. Tianmo, and L. Yijun, *Method for Measuring Relation Curve of Forward Voltage and Junction Temperature of LED (Light Emitting Diode) in lamp*, China Patent CN104748885A, Xiamen University, March, 2010.

39. Chonko, J., *Using Forward Voltage to Measure Semiconductor Junction Temperature*, Keithley Instruments, 2006, https://www.tek.com/en/documents/technical-article/using-forward-voltage-measure-semiconductor-junction-temperature, accessed in January 2022.

40. Shailesh, K. R., C. P. Kurian, and S. G. Kini, "Junction Temperature Measurement of a LED Street Light Using Forward Voltage Method", *International Conference on Advances in Electronics, Computers and Communications*, Bangolore, India, 10-11 October 2014, pp. 1–6, IEEE, 2015.

41. Todoroki, S., M. Sawai, and K. Aiki, "Temperature Distribution Along the Striped Active Region in High-Power GaAlAs Visible Lasers", *Journal of Applied Physics,* vol. 58, no. 3, p. 1124, 1998.

42. Tamdogan, E., G. Pavlidis, S. Graham, and M. Arik, "A Comparative Study on the Junction Temperature Measurements of Leds with Raman Spectroscopy, Microinfrared (IR) Imaging, and Forward Voltage Methods", *IEEE Transactions on Components, Packaging and Manufacturing Technology,* vol. 8, no. 11, pp. 1914–1922, 2018.

43. Sarua, A., H. Ji, M. Kuball, M. J. Uren, T. Martin, K. P. Hilton, and R.S. Balmer, "Integrated Micro-Raman/Infrared Thermography Probe for Monitoring of Self-Heating in AlGaN/GaN Transistor Structures", *IEEE Transactions on Electron Devices*, vol. 53, no. 10, pp. 2438–2447, 2006.

44. Howell, J. R., M.P. Menguc, and R. Siegel, *Thermal Radiation Heat Transfer*, 6th Edition, Taylor & Francis, Boca Raton, 2015.

45. Ozluk, B., A. M. Muslu, and M. Arik, "A Comparative Study for the Junction Temperature of Green Light-Emitting Diodes", *IEEE Transactions on Components, Packaging and Manufacturing Technology,* vol. 9, no. 10, pp. 2024–2035, 2019.

46. Hartmann, J. and S. Völker, “Thermal Management of Light Sources”, *International Journal of Thermophysics,* vol. 32, no. 1–2, pp. 513–522, 2011.

47. Cree LED, *Solder-Point Temperature Measurement of XLamp ® LEDs*, 2013, https://cree-led.com/media/documents/Solder_Point_Temp.pdf, accessed in January 2022.

48. Philips LUMILEDS, *LUXEON S Assembly and Handling Application Brief Confidential AB80 20120227 2*, 2012, http://www.farnell.com/datasheets/1604320.pdf, accessed in January 2022.

49. Kerlin, T. W., *Practical Thermocouple Thermometry*, 2nd Edition, International Society of Automation, Durham, 2012.

50. Fu, X. and X. Luo, “Can Thermocouple Measure Surface Temperature of Light Emitting Diode Module Accurately?”, *International Journal of Heat Mass Transfer*, vol. 65, pp. 199–202, 2013.

51. Lee, D., H. Choi, S. Jeong, C. H. Jeon, D. Lee, J. Lim, C. Byon, and J. Choi, “A study on the Measurement and Prediction of LED Junction Temperature”, *International Journal of Heat Mass Transfer,* vol. 127, pp. 1243–1252, 2018.

52. Lumileds, *How to Measure Thermal Resistance*, 2016, https://lumileds.com/wp-content/uploads/files/WP23.pdf, accessed in January 2022.

53. Andonova, A., N. Kim, and N. Vakrilov, “Estimation the Amount of Heat Generated by LEDs Under Different Operating Conditions”, *Elektronika ir Elektrotechnika*, vol. 22, no. 2, pp. 49–53, 2016.

54. Li, J., Q. Yang, P. Niu, L. Jin, B. Meng, Y. Li, Z. Xiao, and X. Zhang, “Analysis of Thermal Field on Integrated LED Light Source Based on COMSOL Multi-physics Finite Element Simulation”, *Physics Procedia*, vol. 22, pp. 150–156, 2011.

55. Sümer, Y., O. Karaman, and C. Karaman, “Design and Thermal Analysis of High Power LED Light”, *Photonics and Optoelectronic (SOPO),* vol. 5, no. 1, pp. 28–33, 2021.

56. Mashkov, P., T. Pencheva, and B. Gyoch, “LEDs’ Thermal Management Aided by Infrared Thermography”, *Advanced Packaging Materials: Microtech, 2010. APM '10. International Symposium,* Cambridge, UK, 28 February-2 March 2010, pp. 68–73, IEEE, 2010.

57. Comsol, *Semiconductor Module User’s Guide*, 2018, https://doc.comsol.com/5.3/doc/com.comsol.help.semicond/SemiconductorModuleUsersGuide.pdf, accessed in January 2021.

58. Hamida, M. B. B., M.A. Almeshaal, and K. Hajlaoui, “A Three-Dimensional Thermal Analysis for Cooling a Square Light Emitting Diode by Multiwalled Carbon Nanotube-Nanofluid-Filled in a Rectangular Microchannel”, *Advances in Mechanical Engineering,* vol. 13, no. 11, 2021.

59. Chi, W. H., T. L. Chou, C. N. Han, and K.N. Chiang, “Analysis of Thermal Performance of High Power Light Emitting Diodes Package”, *10th Electron. Packaging and Technology Conference*, Singapore, 9-12 December 2008, pp. 533–538, IEEE, 2009.

60. Senawiratne, J., Y. Li, M. Zhu, Y. Xia, W. Zhao, T. Detchprohm, A. Chatterjee, J. L. Plawsky, and C. Wetzel, “Junction Temperature Measurements and Thermal Modeling of GaInN/GaN Quantum Well Light-Emitting Diodes”, *Journal of Electronic Materials*, vol. 37, no. 5, pp. 607–610, 2008.

61. Barbosa, J. L. F., D. Simon, and W. P. Calixto, “Design Optimization of a High Power LED Matrix Luminaire”, *Energies*, vol. 10, no. 5, 2017.

62. Wu, P., R. Fang, X. Dai, and A. A. A. Putri, “Analysis and Optimization of Heat Dissipation Characteristics of High-power LED”, *6th International Conference on Intelligent Information Processing*, New York, USA, 29-31 July 2021, pp. 318–323, Association for Computing Machinery, 2021.

63. Fan, B., H. Wu, Y. Zhao, Y. Xian, B. Zhang, and G. Wang, “Thermal Study of High-Power Nitride-Based Flip-Chip Light-Emitting Diodes”, *IEEE Transactions on Electron Devices*, vol. 55, no. 12, pp. 3375–3382, 2008.

64. Todoroki, S., M. Sawai, and K. Aiki, “Temperature Distribution Along the Striped Active Region in High-Power GaAlAs visible lasers”, *Journal of Applied Physics*, vol. 58, p. 1124, 1985.

65. Datta, S., *Quantum transport: Atom to transistor*, Cambridge University Press, Cambridge, 2005.

66. Goktepe, E. and N. Donmezer, “Current Crowding Effects on the Thermal Performance of AlGaN/GaN Light Emitting Diodes”, *2021 IEEE 23rd Electronics Packaging Technology Conference,* Singapore, 1-4 December 2021*,* pp. 473–478, IEEE, 2021.

67. Turin, V. O. and A. A. Balandin, “Electrothermal Simulation of the Self-Heating Effects in GaN-Based Field-Effect Transistors”, *Journal of Applied Physics,* vol. 100, no. 5, 2006.

68. Bensegueni, R. and S. Latreche, “Numerical method for a 2D drift diffusion model arising in strained n-type MOSFET device”, *Pramana - Journal of Physics*, vol. 86, no. 6, pp. 1391–1400, 2016.

69. Jüngel, A., *Basic Semiconductor Physics*, in Transport Equations for Semiconductors Lecture Notes in Physics, Springer, Heidelberg, 2009.

70. Sentaurus, *Sentaurus Device User Guide*, Synopsys TCAD, CA, 2015

71. Lindefelt, U., "Current-density Relations for Nonisothermal Modeling of Degenerate Heterostructure Devices", *Journal of Applied Physics*, vol. 75, no. 2, p. 958,1998.

72. Marshak, A. H. and C.M. Van Vliet, "Electrical Current and Carrier Density in Degenerate Materials with Nonuniform Band Structure", *Proceedings of the IEEE*, vol. 72, no. 2, pp. 148–164, 1984.

73. Nakamura, S. and J. Piprek, "Physics of High-Power InGaN/GaN Lasers", *IEE Proceedings - Optoelectronics*, vol. 149, no. 4, pp. 145–151, 2002.

74. Malyutenko, V. K., A. D. Podoltsev, and O. Y. Malyutenko, "Current Crowding Impact at Spatially and Temporarily Resolved Thermal Characters of Large-Area AlGaInP Light Emitting Diodes Operating in Dimming/Flashing Modes", *Journal of Applied Physics*, vol. 118, no. 15, p. 153105, 2015.

75. Othman, M. F., S. Ahmad, F. N. A. Saad, A. N. Alias, A. A. Aziz, and M. R. Hashim, "Current Crowding Effect in Lateral and Vertical LED Configurations: 3D Simulation and Characterisation", *IEEE Control System, Computing and Engineering*, Penang, Malaysia, 23-25 November 2012, pp. 530–534, IEEE, 2013.

76. Wang, T., J. Xu, and X. Wang, "Self-heating Dependent Characteristic of GaN-Based Light-Emitting Diodes with and Without AlGaInN Electron Blocking Layer", *Chinese Science Bulletin*, vol. 59, no. 20, pp. 2460–2469, 2014.

77. Hwu, F.S., J. C. Chen, S. H. Tu, G. J. Sheu, H. I. Chen, and J. K. Sheu, "A Numerical Study of Thermal and Electrical Effects in a Vertical LED Chip", *Journal of The Electrochemical Society*, vol. 157, no. 1, p. H31, 2010.

78. Cao, B., S. Zhou, and S. Liu, “Effects of ITO Pattern on the Electrical and Optical Characteristics of LEDs”, *ECS Journal of Solid State Science and Technology*, vol. 2, no. 1, pp. R24–R28, 2013.

79. Shim, J.I., J. Yun, and H. Kim, “Current Spreading and Its Related Issues in GaN-Based Light Emitting Diodes”, *Proc. SPIE 7216, Gallium Nitride Materials and Devices IV,* vol. 7216, pp. 161–169, 2009.

80. Hao, G. D., M. Taniguchi, N. Tamari, and S. I. Inoue, “Enhanced Wall-Plug Efficiency in AlGaN-based Deep-Ultraviolet Light-Emitting Diodes with Uniform Current Spreading p-electrode structures*”, Journal of Physics D Applied Physics,* vol. 49, no. 23, 2016.

81. Wang, C. K., T. H. Chiang, Y. Z. Chiou, and S. P. Chang, “Reducing the Current Crowding Effect on Nitride-Based Light-Emitting Diodes Using Modulated p-Extension Electrode Thickness”, *Japanese Journal of Applied Physics*, vol. 52, no. 1 PART2, 2013.

82. Guo, X. and E. F. Schubert, “Current Crowding and Optical Saturation Effects in GaInN/GaN Light-Emitting Diodes Grown on Insulating Substrates”, *Applied Physics Letters*, vol. 78, no. 21, p. 3337, 2001.

83. Shatalov, M., G. Simin, V. Adivarahan, A. Chitnis, S. Wu, R. Pachipulusu, V. Mandavilli, K. Simin, J. P. Zhang, J. W. Yang and M. A. Khan “Lateral Current Crowding in Ceep UV Light Emitting Diodes Over Sapphire Substrates”, *Japanese Journal of Applied Physics,* vol. 41, no. 8, pp. 5083–5087, 2002.

84. Han, D., J. Shim, D. S. Shin, E. Nam, and H. Park, “Effect of Temperature Distribution and Current Crowding on the Performance of Lateral Gan-Based Light-Emitting Diodes”, *Current Topics in Solid State Physics*, vol. 7. no. 7-8, pp. 2133-2135, 2010.

85. Piprek, J., *Optoelectronic Devices: Advanced Simulation and Analysis*, Springer, New York, 2005.

86. Piprek, J., *Semiconductor Optoelectronic Devices: Introduction to Physics and Simulation*, Academic Press, San Diego, 2003.

87. Wang, T. H., J. L. Xu, and X. D. Wang, "The Effect of Multi-Quantum Barrier Structure on Light-Emitting Diodes Performance by a Non-Isothermal Model", *Chinese Science Bulletin, vol*. 57, no. 30, pp. 3937–3942, 2012.

88. Qin, H., X. Luan, C. Feng, D. Yang, and G. Zhang, "Mechanical, Thermodynamic and Electronic Properties of Wurtzite and Zinc-Blende Gan Crystals", *Materials (Basel)*, vol. 10, no. 12, 2017.

89. Sönmezolu, S., "Investigation of The Entropy and Specific Heat Capacity of GaN Using Incomplete Gamma Functions", *International Journal of Modern Physics*, vol. 22, no. 30, pp. 5349–5355, 2012.

90. Ma, J., X. Wang, B. Huang, and X. Luo, "Effects of Point Defects and Dislocations on Spectral Phonon Transport Properties of Wurtzite GaN", *Journal of Applied Physics,* vol. 114, no. 7, 2013.

91. Dundar, C., D. Kara, and N. Donmezer, "The Effects of Gate-Connected Field Plates on Hotspot Temperatures of AlGaN/GaN HEMTs", *IEEE Transactions on Electron Devices*, vol. 67, no. 1, pp. 57–62, 2020.

92. Palankovski, V., R. Schultheis, and S. Selberherr, "Simulation of Power Heterojunction Bipolar Transistors on Gallium Arsenide", *IEEE Transactions on Electron Devices*, vol. 48, no. 6, pp. 1264–1269, 2001.

93. Paskov, P. P., M. Slomski, J. H. Leach, J. F. Muth, and T. Paskova, “Effect of Si Doping on the Thermal Conductivity of Bulk Gan at Elevated Temperatures – Theory and Experiment”, *American Institute of Physics Advances*, vol. 7, no. 9, p. 095302, 2017.

94. Liu, W. and A. A. Balandin, “Thermal Conduction in $Al_xGa_{1-x}N$ Alloys and Thin Films”, *Journal of Applied Physics,* vol. 97, no. 7, p. 073710, 2005.

95. Beechem, T. E., A. E. McDonald, E. J. Fuller, A. A. Talin, C. M. Rost, J. P. Maria, J. T. Gaskins, P. E. Hopkins, and A. A. Allerman, “Size Dictated Thermal Conductivity of GaN”, *Journal of Applied Physics*, vol. 120, no. 9, p. 095104, 2016.

96. Darwish, A., A. J. Bayba, H. A. and Hung, “Channel Temperature Analysis of Gan HEMT’s with Nonlinear Thermal Conductivity”, *IEEE Transactions on Electron Devices*, vol. 62, no. 3, pp. 840–846, 2015.

97. Vitanov, S., V. Palankovski, S. Maroldt, and R. Quay, “High-temperature Modeling of AlGaN/GaN HEMTs”, *Solid State Electronics,* vol. 54, no. 10, pp. 1105–1112, 2010.

98. Sahoo, B. K., “Effect of Macroscopic Polarization on Thermal Conductivity of InN”, *Journal of Alloys Compounds*, vol. 605, pp. 217–221, 2014.